

Modeling Large Dust Aerosols in the Community Earth System Model

Version 2 (CESM2)

Longlei Li^{1,*}, Natalie M. Mahowald¹, Xiaohong Liu², María Gonçalves Ageitos^{3,4}, Ziming Ke⁵, Danny M. Leung⁶, Carlos Pérez García-Pando^{3,7}, Ron L. Miller⁸, Vincenzo Obiso³, Paul Ginoux⁹, Jasper F. Kok¹⁰, Paola Formenti¹¹, Claudia Di Biagio¹¹, Philip G. Brodrick¹², David R. Thompson¹², Roger N. Clark¹³, Gregory S. Okin¹⁴, Robert O. Green¹², Bo Zhou¹⁴, Samuel Albani¹⁵, and Adeyemi A. Adebisi¹⁶

¹Department of Earth and Atmospheric Sciences, Cornell University, Ithaca, NY, United States,

²Department of Atmospheric Sciences, Texas A&M University, College Station, TX, United States,

³Barcelona Supercomputing Center, Barcelona, Spain,

⁴Department of Project and Construction Engineering, Universitat Politècnica de Catalunya – Barcelona Tech, Terrassa, Spain,

⁵Lawrence Livermore National Laboratories, Livermore, CA, United States,

⁶Atmospheric Chemistry Observations and Modeling Laboratory, NSF National Center for Atmospheric Research, Boulder, CO, United States,

⁷ICREA, Catalan Institution for Research and Advances Studies, Barcelona, Spain,

⁸NASA Goddard Institute for Space Studies, New York, NY, United States,

⁹NOAA Geophysical Fluid Dynamics Laboratory, Princeton, NJ, United States,

¹⁰Department of Atmospheric and Oceanic Sciences, University of California – Los Angeles, Los Angeles, CA, United States,

¹¹Université Paris Cité and Univ Paris Est Creteil, CNRS, LISA, F-75013 Paris, France,

¹²Jet Propulsion Laboratory, California Institute of Technology, Pasadena, CA, United States,

¹³Planetary Science Institute, Tucson, AZ, United States,

¹⁴Department of Geography, University of California, Los Angeles, Los Angeles, CA, United States,

¹⁵Department of Environmental and Earth Sciences, University of Milano-Bicocca, Milan, Italy,

¹⁶Department of Life and Environmental Sciences, University of California Merced, CA, United States.

*Corresponding author: Longlei Li (ll859@cornell.edu)

This paper has been submitted to Journal of Advances in Modeling Earth Systems.

29 **Key Points:**

- 30 • A new model is developed to simulate dust aerosols for a wide distribution of sizes with
31 observational constraints and improved mineralogy
- 32 • Including particles larger than 10 microns in diameter greatly alters simulated dust
33 budgets while not degrading finer dust representation
- 34 • Challenges remain, especially for representing the physical mechanisms that transport
35 super coarse dust in Earth system models

Abstract

Dust aerosols have a wide size distribution from less than 1.0 nm to over 100 μm and dominate the Earth's atmospheric aerosol mass. However, most Earth system models inadequately represent dust aerosols larger than 10 μm in diameter, limiting the accuracy of dust cycle and climatic impact simulations. Here, we introduce a new modeling framework that captures the observed full-size distribution of dust aerosols, incorporating recent advances into a mineral-resolved version of the Community Earth System Model and addressing known issues in previous versions. Comprehensive evaluation against diverse observations of bulk dust and component minerals demonstrates that the model reproduces the observed dust cycle across sizes. Incorporating the previously unrepresented fractions substantially alters dust budget estimates, highlighting potential changes in simulated climatic impacts and underscoring the importance of comprehensive size-resolved dust modeling. Despite these advancements, uncertainties persist. Future developments should address misrepresented physical processes that hinder accurate modeling of the transport of dust aerosols larger than 10 μm in diameter, whose gravitational settling velocity must be reduced by 60% in the new model to match observed size distribution. Expanding observational datasets covering the full-size distribution is also essential to better constrain the dust cycle and improve the representation of dust optical properties and climatic effects.

Plain Language Summary

Mineral dust constitutes the largest mass of airborne particles on Earth. These particles span a wide range of sizes from tiny to giant, but not all sizes play an equally important role. As particles that both scatter and absorb solar and thermal radiation while delivering vital nutrients to ecosystems, mineral dust plays a critical role in various Earth system processes and in projections of future climate changes. However, most Earth system models (ESMs), including the Community ESM Version 2 (CESM2), either neglect or underrepresent particles large than 10 microns in diameter, limiting our understanding of dust's influence on climate. Furthermore, the CESM2 dust module, including its mineral-resolved version used in this study, lacks several key physical processes known to affect dust emission and transport. This study enhances the representation of dust aerosols in the mineral-resolved version of CESM2 by extending the upper

size limit of simulated dust particles to 70 microns at emission and adding omitted physical processes for dust emission based on the latest scientific findings. The updated model is evaluated against a wide range of observations under present-day climate conditions.

1 Introduction

Mineral dust, the most abundant aerosol by mass (Gliß et al., 2021), has diverse climatic impacts (Kok et al., 2023) through direct interactions with radiation, indirectly modifying cloud properties, and by depositing micronutrients (e.g., iron or phosphorus) to marine and terrestrial ecosystems (Jickells et al., 2005; Mahowald, 2011; Mahowald et al., 2010, 2018; Mccutcheon et al., 2021; Meskhidze et al., 2005). Dust influences weather and climate, especially near source regions, and acts as an air pollutant causing transportation hazards (Bhattachan et al., 2019) and impacting human health (Goudie, 2014; Maki et al., 2022; Pérez García-Pando et al., 2014). Accurately quantifying these impacts at large (e.g., continental and global) scales requires models capable of reproducing the spatiotemporal life cycle and physicochemical properties of dust aerosols, which are sensitive to dust size (Mahowald et al., 2014). Such capability, however, remains highly limited, partially due to a lack of high-quality observations (Mahowald et al., 2024) with sufficient coverage to constrain key factors, such as dust size (Baker & Jickells, 2006; Liao & Seinfeld, 1998) and mineral composition (Sokolik & Toon, 1999), which remain especially uncertain (Adebiyi & Kok, 2020; Li et al., 2021; Mahowald et al., 2014).

Dust aerosols, typically represented by multiple modes or bins in Earth system models (ESMs), have a broad size range from just above 0.0 up to hundreds of microns (Adebiyi et al., 2023). Like many other ESMs, various versions of the Community ESM (CESM) have focused on simulating dust particles smaller than 10 μm in geometric diameter (referred to as diameter herein unless stated otherwise; fine: smaller than 1.0 μm , fine/coarse: 1.0 - 5.0 μm , and medium coarse: 5.0 - 10 μm) (Zender et al., 2003), even though dust particles between 10 and 20 μm (super coarse), and even larger than 20 μm (super coarse/giant), has been observed during transport from North Africa to Barbados (Prospero et al., 1970) or East Asia to North Pacific (Betzer et al., 1988). Particles larger than 10 μm in diameter, especially those larger than 20 μm , were assumed to be rare and received less attention, because (1) most of them were thought to be rapidly removed from the atmosphere due to gravitational settling and because they are also

more likely to be removed through below-cloud scavenging (Jones et al., 2022) because of larger size; (2) they were considered less relevant to climate; (3) conventional dry-deposition mechanisms (Petroff & Zhang, 2010; Zender, et al., 2003; Zhang et al., 2001) underestimate their lifetimes and long-range transport (Drakaki et al., 2022; Ginoux, 2003; Ratcliffe et al., 2024); and (4) air quality measurements typically focus on dust particles with diameters smaller than 2.5 μm (particulate matter: $\text{PM}_{2.5}$) and 10 μm (PM_{10}) in diameter (Mahowald et al., 2025).

The conventional assumption of a 10 μm cutoff diameter in the dust size distribution was recognized as insufficient for dust aerosol modeling in a limited number of early studies over two decades ago (Betzer et al., 1988; Mahowald et al., 2005). Such limitation gains more attention following recent campaign measurements using in situ and remote sensing instruments (Van Der Does et al., 2016; Ryder et al., 2013, 2019; Ryder et al., 2018; Weinzierl et al., 2017; Weinzierl et al., 2009). These measurements indicate that dust aerosols with diameters larger than 10 μm and up to 40 μm are observed in downwind regions up to 2000 km from North Africa (van der Does et al., 2018). A synthesis of model and observational data highlights that dust particles in the 10 - 20 μm diameter range greatly contribute to regional deposition in areas such as the Southern Ocean (Adebiyi et al., 2023).

Most current ESMs, including CESM with either Bulk Aerosol Module (BAM) (Adebiyi & Kok, 2020) or Modal Aerosol Module (MAM) (Li et al., 2022; Liu et al., 2016), underestimate the abundance of dust particles larger than 5.0 μm in diameter (Adebiyi & Kok, 2020), and even more so for particles larger than 10 μm involved in long-range transport (Ratcliffe et al., 2024), compared to observations. This underrepresentation can potentially bias previous estimates of dust aerosol budgets (e.g., smaller cutoff sizes may result in lower emission mass fluxes, or attribute too much dust to the fine fraction) and assessments of dust impacts on Earth-climate-human interactions (Kok et al., 2023).

To date, only a few studies have attempted to simulate the full-size distribution of dust particles in either regional (Drakaki et al., 2022) or global ESMs (Ginoux, 2003; Ratcliffe et al., 2024; Wang et al., 2024), and even fewer in CESM (Meng et al., 2022), although some other ESMs have a dust cutoff size larger than 10 μm in diameter (Gonçalves Ageitos et al., 2023; Klose et al., 2021; Obiso et al., 2024; Perlwitz et al., 2015a). Most CESM-based dust modeling studies have not adequately included particles larger than 10 μm in diameter (Albani et al., 2014; Li et

al., 2022; Meng et al., 2022). This is because they used older model versions or focused on specific objectives that addressed only limited aspects of dust cycle modeling. For example, Meng et al. (2022) did not focus on model developments within CESM (version 1) but rather on achieving an emitted size distribution consistent with observed dust fluxes. Consequently, their study did not extend model-data comparisons to other critical dust properties, such as surface concentrations, optical depth, and deposition, all of which warrant further investigation. Ke et al. (2022) extended the maximum dust diameter to 20 μm but did not account for coarser aerosols, which remain abundant and are observed downwind of North Africa. The size distribution simulated by their model also requires evaluation against observations, which are unfortunately lacking, before a reliable assessment of the contribution of dust particles between 10 and 20 μm in diameter can be made. There, thus, remains a need for the development of a more comprehensive and precise representation of the dust cycle, which adequately incorporates the dynamics of giant dust particles, along with measurements for evaluating such a model.

The primary objective of this study is to advance the mineral-resolved CESM2 (Li et al., 2022) to comprehensively represent dust aerosols across a wide size range, up to 70 μm in geometric diameter at emission (slightly above the diameter boundary between sand and dust particles at 62.5 μm). To achieve this, we develop a ten-mode MAM (MAM10) and constrain the simulated dust size distribution with observations. We also incorporate recent developments into this more comprehensive framework to simulate the climatic impacts of dust aerosols.

Specifically, this study introduces several key developments:

(1) The new MAM10: We develop this new aerosol module to include dust particles larger than 20 μm and up to 70 μm in geometric diameter upon emission within the mineral-resolved Community Atmosphere Model Version 6 (CAM6) framework (Li et al., 2022) as an extension to the CAM5-MAM9 (Ke et al., 2022), which lacks mineral speciation. The mixing state of dust aerosols with non-dust aerosols, such as sea salt, has been revised as well. The simulated dust size distribution is constrained by comprehensive measurements including the super coarse and giant dust fractions (Formenti & Di Biagio, 2024).

(2) Improved dust emission scheme: We improve the dust emission scheme in the mineral-resolved CESM2 by adding drag partitioning by non-erodible elements (e.g., rocks and

vegetation) and intermittency due to the coarse temporal resolution of the model relative to the timescale of surface wind oscillations (Leung et al., 2023).

(3) Updated soil mineralogy atlas: We incorporate a new atlas from the Earth surface Mineral dust source InvesTigation (EMIT) project (Green et al., 2020) to characterize mineralogy in current and potential future erodible soils. Prior to the EMIT mission, dust source composition was estimated from two highly uncertain global soil atlases based on limited mineral measurements and, heavily interpolated over the non-agricultural regions that are the key dust source areas (Claquin et al., 1999; Journet et al., 2014) (pre-EMIT soil mineral atlases). The new EMIT soil mineral atlas produced the first global-scale mineral atlas of dust source regions based upon direct measurements. This EMIT dataset has been shown to significantly reduce uncertainties in dust mineral composition and, consequently, in the simulated dust shortwave direct radiative effect for both the present day and projections for the late 21st century, relative to simulations using pre-EMIT soil atlases (Li et al., 2025).

(4) Updated optics for iron oxides: We modify the optics for iron oxides using observationally constrained values, which have been shown to capture both the laboratory-measured dust aerosol optics and their relationship with iron oxide content (Li et al., 2024).

This paper evaluates the performance of the new mineral-resolved CESM2 in simulating key features of the observed dust cycle. We also quantify the simulated dust budget, including the contribution of newly incorporated super coarse and giant dust particles. Our analysis focuses on the updated model, with comparisons made to the previous version (Li et al., 2022), without attributing improvements to specific model developments.

2 General Model Overview and Treatments in Previous Versions

We utilize the National Center for Atmospheric Research CESM version 2.1.0 (CESM2.1.0). This model comprises multiple components, including the atmosphere component (CAM6) and the land component (Community Land Model version 4.5; CLM4.5), crucial for representing Earth's processes in climate projections.

Parameterizations for eolian processes responsible for dust emission are primarily implemented in CLM4.5, which communicates with CAM6 through a coupler, transmitting vertical emission

fluxes. CAM6 then redistributes the emission flux into different aerosol modes when employing a MAM, and simulates the transport, deposition, and radiative impacts of dust aerosols.

2.1 Modal Aerosol Module

CAM6 by default utilizes a four-mode MAM (MAM4) (Liu et al., 2016) to represent a total of six aerosol species: Aitken (A2: soil dust, sulfate, sea salt, and secondary organic matter), accumulation (A1: sulfate, secondary organic matter, primary organic matter, black carbon, sea salt, and soil dust), coarse (A3: soil dust, sea salt, and sulfate), and a primary carbon mode (A4: primary organic matter and black carbon). These species, represented by separate tracers, are assumed to be internally mixed within the same mode and externally mixed between different modes. Due to the varying physical properties of species (e.g., hygroscopicity, optical properties, and density), this aerosol mixing state is essential for accurately modeling the full aerosol cycle and diagnosing optical properties, which influence radiative effect estimates. In addition, the total number concentration of aerosol species in a mode is also advected as a separate tracer, along with the mass mixing ratio of each species (Liu et al., 2016).

The size distribution of each mode assumes a log-normal shape, with the mode parameters listed in Table 1. These parameters are prescribed in the user namelist file, including the globally constant geometric standard deviation, the initialized geometric mean diameter for online predictions, and the range used to constrain the simulated geometric mean diameter. It is worth noting that a previous study (Li et al., 2022) adjusted the coarse mode size distribution parameters (geometric standard deviation, initialized geometric mean diameter, and its range) to those used in CAM5, leading to large changes in the modeled dust aerosol cycle and improving the representation of the dust size distribution. This adjustment is retained here to better represent the dust aerosol size distribution in CAM6-MAM4.

211 **Table 1.** *Dust Mode Parameters in MAM4.*

Dust Modes		A1	A2	A3
		(Aitken)	(Accumulation)	(Coarse)
Emitted Geometric Diameter Limits (μm) for Mass-to-Number Flux Conversions		0.010 - 0.10	0.10 - 1.0	1.0 - 10
Geometric Standard Deviation		1.6	1.8	1.8
Initialized Dry Geometric Mean Diameter (μm) for the Number Distribution		0.026	0.11	2.0
Low and Upper Bounds for Simulated Dry Geometric Mean Diameter (μm ; Number Distribution)		0.0087 - 0.052	0.054 - 0.44	1.0 - 4.0
Emitted mass fractions	Fractional Contribution to Total Dust	0.0010	0.011	0.99
	From Clay	1.0	1.0	0.69
	From Silt	0.0	0.0	0.31

212 Processes that determine the removal rate of aerosols from the atmosphere include dry and wet
 213 deposition. The dry deposition (e.g., gravitational settling and turbulent removal) rate, calculated
 214 in the model via parameterizations, partially depends on the aerosol size (i.e., the predicted
 215 geometric mean diameter and geometric standard deviation for each mode). The model we take
 216 as default here uses a revised dry deposition scheme (Petroff & Zhang, 2010), compared to that
 217 used in the officially released version (Zhang et al., 2001). This revised scheme, as previously
 218 shown, helps mitigate the overestimated dry deposition velocity of fine aerosols, such as black
 219 carbon (Wu et al., 2018) and dust in the fine modes (Aitken plus accumulation) (Li et al., 2022),
 220 as tested in CAM5 and CAM6 (officially released versions), respectively.

221 Wet deposition depends on the relative location of aerosols to clouds. It consists of in-cloud and
 222 below-cloud scavenging, both of which are applied separately to convective and stratiform
 223 precipitation. The in-cloud scavenging uses cloud properties (e.g., cloud water, precipitation
 224 production profiles) to compute aerosol loss rates, scaled by solubility factors that represent the
 225 aerosol fraction incorporated into cloud water. Stratiform cloud-borne aerosols have a solubility
 226 factor of 1.0 for all activated aerosols, while interstitial aerosols are unaffected. Convective in-

cloud scavenging applies solubility and activation factors specific to aerosol mode (0.40 for dust) and hygroscopicity (0.068), with lower activation values for less hygroscopic modes.

The below-cloud scavenging removes interstitial aerosols through impaction and diffusion, with removal rates dependent on solubility factor, scavenging coefficient, and precipitation rate (Neale et al., 2010). CAM6-MAM4 calculates size-dependent scavenging coefficients (Easter et al., 2004) and applies a solubility factor of 0.10, which effectively serves as a tunable parameter. Stratiform cloud-borne aerosols are not subject to the below-cloud scavenging. However, aerosols scavenged at higher altitudes can be resuspended at lower atmospheric levels. In CAM6, the fraction of resuspended aerosol is set equal to the fraction of evaporated precipitation.

A particle's hygroscopic growth or shrinkage depends on its hygroscopicity, dry radius, density, ambient relative humidity, and temperature, following the κ -Köhler theory (Ghan and Zaveri, 2007). This process determines the particle's final wet size and volume at equilibrium under ambient conditions. The volume-averaging mixing rule is then applied to predict the band-averaged (see Li et al., 2021 for band information) complex refractive index of the wet aerosol mixture, based on the relative abundance and refractive index of each component (using its dry-state value for aerosols), including water (Ghan and Zaveri, 2007). To parameterize the optical properties of the aerosol mixture, such as single-scattering albedo across different bands, the model uses a look-up table containing Chebyshev polynomial coefficients (see Section 3.1.3 for details on how we generate it) and an interpolation method based on the band-averaged complex refractive index of the wet aerosol mixture (Ghan and Zaveri, 2007).

2.2 Default Dust Modeling Without Mineral Speciation

The default dust emission in the officially released CESM2 relies on the dust entrainment and deposition model (DEAD) (Zender et al., 2003) in CLM4.5, which simulates the dust mobilization based on the mechanism proposed by Marticorena and Bergametti (1995). This emission scheme was previously updated to a more physically based one (Kok, et al., 2014), shifting emissions to topographic depressions, where abundant erodible sediment accumulates,

without using a time-invariant empirical source function such as previously used (Ginoux et al., 2001; Mahowald et al., 2006; Zender et al., 2003).

Dust emission is initiated when the near-surface friction velocity exceeds the fluid soil threshold friction velocity for saltation, the process by which wind lifts sand particles (100 μm) and propels them into ballistic trajectories, ejecting smaller dust aerosol-sized particles into the air upon collision (Kok et al., 2012). This soil threshold friction velocity is determined primarily by near-surface meteorological fields and top 1.0 - 2.0 cm soil properties such as moisture content, grain size distribution, and land cover (e.g., vegetation) (e.g., Shao, 2008). Vegetation influences dust emissions via the leaf area index (Mahowald et al., 2006) in CLM4.5. When the leaf area index exceeds $0.30 \text{ m}^2 \text{ m}^{-2}$, vegetation is assumed to fully block the transfer of wind momentum to the surface soil, preventing dust emission. Below this threshold, the fraction of a grid cell that can emit dust aerosols increases linearly with decreasing leaf area index. The suppression of dust emissions due to soil moisture is activated when the near-surface soil gravimetric water content exceeds a threshold determined by the clay content of the soil. This relationship is represented in the land model using a semi-empirical formulation (Fécan et al., 1998) and the top 10 cm soil gravimetric water content. Observational studies linking wind threshold behavior to soil gravimetric water content typically focus on the top 1.0 - 2.0 cm of soil, which dries rapidly following precipitation. In contrast, the uppermost soil layer in the model spans 0.0 - 10 cm and retains moisture longer, introducing inertia not representative of surface conditions and thus uncertainty in the dust emission modeling (Darmenova et al., 2009), which we do not address in this study.

The size distribution of emitted total dust aerosols follows the brittle fragmentation theory (Kok, 2011a), which allocates 0.10, 1.0, and 98.9% of dust mass into Aitken, accumulation, and coarse modes, respectively, regardless of the friction velocity at the time of emission (Kok, 2011b). After emission, dust aerosols are transported, interacting with radiation and clouds, and removed from the atmosphere in CAM6.

Evaluations using observations, including in situ measurements and remote sensing retrievals, suggest that compared to the default emission scheme in the officially released CAMs (Zender, Bian, et al., 2003), the more physically based emission scheme, along with the updated size

distribution of emitted total dust aerosols, maintains or improves accuracy in modeling the dust climatology in previous CAM versions (Kok, Albani, et al., 2014; Li et al., 2022).

2.3 Mineral-Resolved Dust Modeling

The dust model (Section 2.2) was modified to categorize the single dust tracer into eight separate mineral tracers (Li et al., 2021; Scanza et al., 2015), enabling detailed optical property calculations based on dust mineral composition. The eight minerals include illite, kaolinite, montmorillonite (smectite), iron oxides (hematite + goethite), quartz, calcite, feldspar, and gypsum. They represent the most common clay- (soil grain diameter below 2.0 μm) and silt-sized (diameter between 2.0 - 63 μm) soil categories (Claquin et al., 1999).

The distribution of the eight minerals in the clay- and/or silt-sized categories was derived offline from a global soil atlas, based on the mean mineralogy table of Claquin et al. (1999), where mineralogy is inferred from a global atlas of soil type. Additional modifications by Scanza et al. (2015) and Li et al. (2021) include normalizing the mineral fractions within each clay- or silt-sized category for 28 soil types. An equal and opposite adjustment to the illite percentage ensures consistent hematite amounts in both clay- and silt-sized categories. A nearest-neighbor algorithm was then applied to fill the grid cells in the land model for dust emission. The conversion of soil mineralogy to dust aerosol mineralogy follows the brittle fragmentation theory (Kok, 2011a), as previously described (Scanza et al., 2015).

The mass distribution of each mineral across the three emission modes matches that of the model without mineral speciation (Section 2.2). Each mineral, treated as a separate tracer, undergoes the same processes as dust in the released model version, including advection, deposition, and aerosol microphysics (e.g., coagulation).

All component minerals are assumed to be internally mixed within a mode. Mineral densities are set to values used in a previous study (Li et al., 2021). The scavenging efficiency and hygroscopicity of these minerals are consistent with those prescribed for dust without speciation, as described in Section 2.1. The complex refractive indices for all component minerals, except iron oxides, are based on Scanza et al. (2015). For iron oxides, an observationally constrained refractive index is applied, which improved the accuracy in predicting optical properties of dust

aerosols using the volume-averaging mixing rule, compared to other publicly available indices (Li et al., 2024).

3 Updates to Dust Representations in the Model

We introduced two key enhancements to the mineral-resolved CAM6: additional modes via the new MAM10 to simulate super coarse and giant dust particles (Section 3.1) and improved physics to model dust emission (Section 3.2). The development of MAM10 in CAM6 builds upon the previous MAM9 and MAM7 frameworks in CAM5 (Ke et al., 2022; Liu et al., 2012) without mineral speciation, while the advanced dust emission physics are based on those implemented in CAM6 (Leung et al., 2024), which likewise has no mineral speciation. The first modification primarily involves changes to the atmosphere component, and the second focuses on the land component.

3.1 A New Modal Aerosol Module

MAM10 represents dust aerosols in five distinct transport modes (A5, A7, A8, A9, and A10), as summarized in Table 2. Each of these modes contains two internally mixed species: dust and sulfate. While we do not detail sulfate representations, we note that sulfate has multiple sources (Liu et al., 2012), and that sulfate in the coarse modes originates from the condensation of sulfuric acid gas produced by the oxidation of sulfur dioxide, which is either directly emitted or formed via the oxidation of dimethyl sulfide. Sea salt is represented in A1, A2, A4, and A6, separate from dust modes, similar to MAM7 and MAM9 (Ke et al., 2022; Liu et al., 2012). Other non-dust aerosol species, such as particulate organic matter and black carbon in the non-dust accumulation mode (A2) aged from the primary carbon mode (A3), are also simulated in MAM10 using the same mode settings as in MAM9.

It is important to note that simulations of the non-dust species in MAM10 are expected to vary from MAM4 due to different size settings and mixing states of dust aerosols with the other species (e.g., sea salt). These distinctions could affect the simulated dust aerosols by modifying dust deposition rates. For example, the internal mixing of sea salt with dust aerosols can increase the hygroscopicity of the mixture, thereby enhancing the wet removal rate of dust aerosol. The simulation of non-dust aerosol species, their climatic impacts, and their influence on dust aerosol

simulations fall outside the scope of this study.

Table 2. *Dust Mode Parameters in MAM10.*

Dust modes		A5	A7	A8	A9	A10
		(Fine)	(Fine/Coarse)	(Medium Coarse)	(Super Coarse)	(Super Coarse/Giant)
Dust Emission Size	Cut-offs (μm)	0.10 - 1.0	1.0 - 5.0	5.0 - 10	10 - 20	20 - 70
Geometric Standard Deviation (GSD)		1.8	1.7	1.5	1.5	1.5
Initialized Dry Geometric Mean Diameter (GMD; μm) (Number Distribution)		0.56	2.0	5.5	8.6	14
Low and Upper Bounds for Simulated Dry GMD (number distribution; μm) ^a		0.36 - 0.76	1.7 - 2.4	4.0 - 6.3	8.3 - 10	10 - 18
Emitted Mass	Fractional Contribution to Total Dust	0.0028	0.14	0.19	0.24	0.43
Fractions	From Clay	1.0	0.97 (0.57) ^b	0.87 (0.57) ^b	0.87	0.87
	From Silt	0.0	0.030 (0.43) ^b	0.13 (0.43) ^b	0.13	0.13

Note. ^a Lower and upper bounds are applied to constrain the simulated geometric mean diameter of each dust mode. ^b Values outside parentheses are derived using the brittle fragmentation theory for non-hematite minerals, while values in parentheses correspond to hematite and have been refined.

As in previous MAM versions, each mode is described by three parameters: the geometric standard deviation, geometric mean diameter, and volume or mass concentration, detailed in Tables 1 and 2 and the following subsections.

3.1.1 Refinement of Dust Size Distribution

The mode parameters (Table 2), along with adjustments to the dry settling velocity of dust aerosols (Table 3), were fine-tuned to match the observed size distribution (Formenti & Di

Biagio, 2024). The optimized dust aerosol size distribution from Adebiyi and Kok (2020), extended to include the giant dust mode (emission size range in geometric diameter: 20 - 70 μm), supports using a constant standard deviation of 2.0 across all modes. However, initial tests with this value failed to match observations near North African dust sources, whereas a subsequent test, reducing the standard deviation to 1.5 for the three largest dust modes (A8, A9, and A10; Table 2), achieved a better model performance (see Section 7.2.3).

The rationale for adopting a geometric standard deviation of 1.5, rather than 2.0, which provides the best fit to the observed size distribution using five lognormal modes, likely reflects persistent uncertainties in dust modeling and model-observation comparisons. For example, modeling the evolution of dust size remains inherently challenging. We applied the obtained geometric standard deviation uniformly in all the calculations requiring this parameter, including diagnostics of dust optical properties. The assumption behind using a constant geometric standard deviation across different modes globally is that the width of the size distribution remains unchanged between freshly emitted and aged dust aerosols. This approach may not fully capture variations in the geometric standard deviation, as atmospheric processes (e.g., size-dependent cloud interactions and deposition) can modify the size distribution during transport. A more accurate solution would be desirable as the model development advances with additional measurements of both freshly emitted and aged dust aerosols.

While the mode parameters for dust between 0.40 and 10 μm are relatively well constrained by observations, those for particles outside this range are more uncertain (Formenti & Di Biagio, 2024). This reduced confidence for the submicron accumulation mode stems from several factors, including contamination by non-dust aerosols (e.g., biomass burning, especially for particles smaller than 0.50 μm in diameter) and assumptions about dust shape that limit the accuracy of the measurements used for size distribution optimization (Dubovik et al., 2000). For the giant dust mode, the uncertainty is mainly due to the scarcity of measurements and instrument limitations. Although AEROSOL ROBOTIC NETWORK (AERONET) retrievals are abundant and capture aerosol mass up to 30 μm in diameter, they are sensitive to assumptions about large particle sizes.

Due to challenges in representing the dust size distribution, the model requires a prescribed range of the geometric median diameter for each mode to reasonably simulate it. Sensitivity tests

without these bounds show that the last four largest dust modes (A7, A8, A9, and A10) tend to merge into a single broad mode. The geometric mean diameters of the fine/coarse and medium-coarse modes are sensitive to the prescribed upper bounds, while the super coarse and giant modes are more influenced by the lower bounds. Limited observational data to constrain the simulated diameters for the three largest dust modes (A8, A9, and A10), combined with the use of a globally constant geometric standard deviation for each mode and the absence of mechanisms to transport dust particles larger than 5.0 μm in diameter, prevents this study from fully capturing the observed dust size dynamics.

3.1.2 Tuning the Gravitational Settling Velocity for Large Dust Particles

The Stokes settling velocity overestimates the settling velocity of particles larger than 20 μm in diameter by more than 10%, primarily because the particle Reynolds number (Re) approaches or exceeds 1.0, the upper limit for which Stokes' law is valid (Stokes, 1851). The magnitude of this error becomes more pronounced with increasing dust particle size. For example, particles of 200 μm in diameter can have a settling velocity bias of up to 60%. To address this issue, a time-invariant Stokes correction factor was applied in CAMs to coarse particles up to a maximum aerosol diameter of 1000 μm (Zender et al., 2003), although previous versions of CAM did not simulate aerosol particles of such large sizes. Despite this correction, large dust particles still appear to settle too quickly compared to the real atmosphere, limiting the model's ability to match measured dust size distributions (see discussions in Section 8 for the proposed reasons so far).

Due to misrepresented or absent mechanisms in the model's dust-related parameterizations, an adjustment, as applied in previous studies (Drakaki et al., 2022; Meng et al., 2022), is used to better simulate coarse dust aerosols. Specifically, we reduce the settling velocity for the three largest dust modes (A8, A9, and A10) by 50, 75, and 85%, respectively (Table 3), to counteract gravitational settling, thereby narrowing the differences in dust size distribution between the model and observations. While more formal alternative methods may exist (see discussions in Section 8), this approach offers a practical compromise to address the overestimation of coarse dust particle settling velocity in the models until particle transport mechanisms are better understood and incorporated, a critical task beyond the scope of this study.

409 **Table 3.** *Experimental Design.*

Mode version	MAM4	MAM10
Emission Scheme	Kok et al. (2014); linear dependency on modeled LAI and the threshold LAI is set as 0.30 m ² /m ² above which no emission occurs	Leung et al. (2023; 2024) with MERRA2 LAI and increased threshold LAI to 1.0 m ² /m ²
Size Distribution	As in Li et al. (2022); also shown in Table 1	See Table 2
Dust Tuning Parameter (dust_emis_fact: Inversely Linked to Dust Emission Rate)	3.6	0.35
Dust Optical Depth in the Visible Band (0.44 - 0.63 μm)	0.030	0.031
Percentage Reduction to Gravitational Settling Velocity of Dust Aerosol	0.0	50, 75, 85 for A8, A9, and A10, respectively
Simulation Period	2007 - 2011 (one additional year for model spin-up)	2007 - 2011 (one additional year for model spin-up)
Look-Up Table for Aerosol Optic Diagnostics	As in Li et al. (2022)	Regenerated to accommodate with new dust modes (Sect. 3.1.3)
Soil Atlases	Mineral fractions derived from Claquin et al. (1999) and normalized to unity	Derived from EMIT following ATBD (see Section 3.4)

410 *Note.* Abbreviations: MAM - Modal Aerosol Module; LAI - Leaf Area Index; MERRA2 -
411 Modern-Era Retrospective analysis for Research and Applications Version 2; EMIT - Earth
412 surface Mineral dust source InvesTigation; ATBD - Algorithm Theoretical Basis Document.

413 Changes in the gravitational settling velocity of coarse mode aerosols can also influence their
414 wet deposition processes, which we do not quantify separately from the total dust budget
415 estimation, including dry deposition. This interaction arises for two main reasons. First,

modifying the dry deposition velocity in a coarse mode can alter simulated dust burdens, which directly affect the wet scavenging rate as a first-order function of dust burden, thereby impacting dust aerosol removal via wet deposition. Second, due to the mode's width, dust number or mass concentrations in one mode can contribute to the total dust mass within the size range represented by neighboring modes. This contrasts with the binned approach, where size bins have fixed boundaries and no overlap between modes.

3.1.3 Parameterization of Aerosol Optical Properties

CAM6 uses parameterized aerosol optical properties to calculate aerosol radiative effects while minimizing computational costs. In this study, we use the approach outlined by Ghan and Zaveri (2007), generating a coefficient look-up table for MAM10. Sensitivity tests by Ghan and Zaveri (2007) suggest that this method reproduces aerosol optical properties calculated by the Mie Theory with errors generally less than 20%, and under most conditions, within 30% of the Mie solution, except when their absolute values are small.

The look-up table, applied to all aerosol modes and species, provides coefficients for total aerosol specific absorption (σ_{abs}), extinction (absorption plus scattering, σ_{ext}), and the asymmetry parameter (g) across 14 shortwave bands, as well as specific absorption for 16 longwave bands. We derive the coefficients by fitting Chebyshev polynomials to mass-weighted (m_w) specific optical properties (i.e., $\log(\sigma_{\text{sca}}/m_w)$, σ_{abs}/m_w , and g) based on Mie simulations with seven real (n_r) and ten imaginary (n_w) components of refractive indices that bracket the probable absorption range of aerosols. These components are equally spaced between 1.3 - 1.6 and 0.0 - 0.79, respectively. A brief introduction to the parameterization of aerosol optical properties using the Mie Theory is provided in Text S1 in Supporting Information, with detailed descriptions available in Ghan and Zaveri (2007).

It is important to note that the Mie Theory cannot be applied to particles with non-spherical shapes for optical property calculations. However, dust aerosols are typically non-spherical (Kalashnikova & Sokolik, 2004) and exhibit complex morphologies (Falkovich et al., 2001), which increase their extinction efficiency (Huang et al., 2023). To address this limitation, we apply shape corrections by increasing the mass extinction efficiency by 16% for fine dust aerosols (A5 and A7) and by 28% for coarser dust aerosols (A8, A9, and A10), based on

previous calculations (Kok et al., 2017) and an extension of the dust emission cutoff geometric diameter to 70 μm . This adjustment is applied only to shortwave bands, as the dust model is tuned to the estimated global visible-band dust optical depth of 0.030 (Ridley et al., 2016), although shape effects may similarly enhance the longwave extinction efficiency (Huang et al., 2023).

3.2 Amendments to Dust Emission Physics

Despite the improvements achieved (Kok, et al., 2014), the physically based scheme previously incorporated into the mineral-resolved CESM2-CAM6 (Li et al., 2022) (described in Section 2.2) still lacks key physics necessary for accurately predicting dust emission strength and location. This limitation led to the development of a more scientifically comprehensive scheme (Leung et al., 2023) designed for integration into ESMs (Leung et al., 2024). Here, we incorporate this scheme into our mineral-resolved dust model.

The additional physics included in the emission process now accounts for two critical factors. First, intermittency from unresolved instantaneous wind fluctuations, such as turbulence, which occur on timescales (around one minute or less) smaller than the model's 30-minute time step within the near-surface boundary layer. Second, drag partitioning due to surface roughness elements, like vegetation and rocks, that partially absorb wind momentum. This absorption reduces the downward momentum flux available to uplift soil dust particles.

We briefly summarize the key elements below. Texts S2 and S3 in Supporting Information provide additional details on the parameterizations of emission intermittency and drag partitioning due to non-erodible elements, respectively. For further information, see Leung et al. (2023).

Moreover, a global unconsolidated sediments map (GUM) (Börker et al., 2018) is applied as a surface erodibility constraint in the updated dust emission model. This implementation suppresses dust emission from consolidated surfaces, allowing emission only from unconsolidated regions (e.g., loose sands, silts, and dust beds) and spectrally identified by EMIT as potential dust sources.

3.2.1 Emission Intermittency

In ESMs with prognostic dust, accounting for intermittency could be crucial (Comola et al., 2019) to avoid considerable biases in dust emission simulations (Dupont et al., 2013). Saltation intermittency is due to the highly turbulent surface winds that frequently sweep across the dust emission threshold friction velocity, causing multiple sudden initiations and terminations of dust emission on a timescale of minutes. Theoretical studies indicate that the saltation intermittency effect is further complicated by the fact that there are two threshold friction velocities for dust emission: the fluid threshold required to initiate saltation, and the impact threshold required to sustain saltation after it has been initiated (Bagnold, 1941; Kok et al., 2012). In most schemes, dust emission begins when friction velocity exceeds the fluid threshold but ceases when friction velocity falls below this threshold. However, in practice, emission persists even when friction velocity decreases to a value between the two thresholds, ceasing only when it drops below the impact threshold. This saltation intermittency effect could be important under two conditions where accounting for intermittency can improve dust emission simulations (Kok et al., 2012).

First, when the model surface wind speed is below the fluid erosion threshold, turbulent fluctuations can still initiate saltation and dust emission, which is then sustained until the wind drops below the impact threshold. Second, soil cohesion, while not affecting the impact erosion threshold, considerably increases the fluid erosion threshold (Comola et al., 2019). These conditions typically occur in marginal source regions (e.g., semi-arid areas) due to higher soil moisture than arid regions. Consequently, incorporating the intermittency effect tends to increase dust emissions over these marginal source regions more than over arid regions (Leung et al., 2023).

To include the intermittency effect, a substepping scheme was developed to parameterize the effects of instantaneous wind fluctuations on initiating and ceasing dust emission (Comola et al., 2019). A saltation intermittency factor, ranging between 0.0 and 1.0, is introduced in the updated dust emissions scheme (Leung et al., 2023), representing the fraction of time during which saltation and dust emissions are active within a model time step (see Text S2 in Supporting Information). The updated dust emission is then modeled as the product of this intermittency

factor and the vertical dust emission calculated by the previous version of the scheme for each model time step.

3.2.2 Drag Partitioning Due to Non-Erodible Elements

A surface roughness correction factor is applied to the modeled friction velocity to account for drag partitioning effects from rocks or vegetation (Leung et al., 2023), which were either absent or not well represented in CESM versions before that study. The effects of these two elements are calculated separately and then combined using a weighted mean based on the fractional area of each grid cell dominated by rocks or vegetation (see Text S3 in Supporting Information).

The drag partitioning due to rocks is quantified using a semi-empirical equation by Marticorena and Bergametti (1995), with aeolian roughness length provided by satellite retrievals of the backscatter coefficient at 5.3 GHz (Prigent et al., 2005). To separate the roughness map for rocks from vegetation, the minimum value of the monthly aeolian roughness length in a climatological year was used. This map is applied to grid cells where the vegetation area index (the sum of the one-sided leaf area index and stem area index) is less than $1.0 \text{ m}^2 \text{ m}^{-2}$. The parameterization thus accounts only for photosynthetic vegetation, excluding other types such as plant debris and senescent leaves.

The drag partitioning due to vegetation is parameterized following Pierre et al. (2014), building on Okin (2008), by using a gamma distribution to represent the gaps between plants. This parameterization is straightforward to implement in ESMs, as drag partitioning can be approximated using only the leaf area index. In the simulation with the updated model here, the leaf area index is taken from the Modern-Era Retrospective analysis for Research and Applications Version 2 (MERRA2) (Gelaro et al., 2017).

3.3 Conversion of Soil Mineralogy to Aerosol Mineralogy

The distribution of emitted minerals across five dust aerosol modes is determined using the extended brittle fragmentation theory (Meng et al., 2022) and the method proposed by Scanza et al. (2015). The original brittle fragmentation theory predicts that the emitted particle size distribution follows a power law for dust particle diameters (D_d) between 2.0 and 10 μm , with emission outside this range determined by the size-crack propagation length (λ). In contrast to

Scanza et al. (2015), our calculation of the emitted mineral distribution employs the bulk dust distribution derived by Meng et al. (2022), which accounts for the dependence of the size-crack propagation length on the diameter of soil aggregates (diameter D_{agg}), in addition to the fully dispersed soil size distribution used in Kok (2011a) and Scanza et al. (2015). This new approach yields a mineral size distribution consistent with the bulk dust distribution used in our model. However, the dispersed soil size distribution is treated as a free parameter, determined by fitting the emitted dust size distribution to observations. The resulting soil particle distribution is skewed toward finer sizes, potentially overrepresenting the clay-sized fraction relative to the parent soil. In contrast, minerals more evenly distributed across both clay- and silt-sized fractions, such as iron oxides, are less sensitive to the assumed soil size distribution.

Following Meng et al. (2022), Equation 1 expresses the size-crack propagation length which is proportional to the size of the fragmented soil dust aggregate:

$$\lambda = f_{\lambda} D_{agg}, \quad (1)$$

where f_{λ} , the ratio of the size-crack propagation length to the dust aggregate size, is set to 0.15.

The normalized emitted mass (M_d) particle size distribution accounting for soil aggregation is given by Equation 2:

$$\frac{dM_d}{d\ln D_d} = \frac{D_d}{C_m} \left[1 + \operatorname{erf} \left(\frac{\ln(D_d/\overline{D_s})}{\sqrt{2}\ln(\sigma_s)} \right) \right] \int_0^{\infty} \exp \left(-\frac{D_d}{f_{\lambda} D_{agg}} \right)^3 P_{agg}(D_{agg}) dD_{agg}, \quad (2)$$

where erf is the error function, and C_m is a normalized constant ensuring unit integral of Equation 1 over the size range of 0.10 - 70 μm . The size distribution of fully dispersed soil is approximated by a lognormal distribution with a volume median diameter $\overline{D_s} = 1.13 \pm 0.58 \mu\text{m}$ and a geometric standard deviation $\sigma_s = 1.9 \pm 0.25$. The size distribution of fragmented soil dust aggregates is also modeled as a log normal distribution with a volume median diameter $\overline{D_{agg}} = 127 \pm 47 \mu\text{m}$ and a geometric standard deviation $\sigma_s = \sim 3.0 \pm 1.0$:

$$P_{agg}(D_{agg}) = \left[\frac{1}{D_{agg} \ln(\sigma_{agg}) \sqrt{2\pi}} \right] \exp \left[-\frac{(\ln(D_{agg}/\overline{D_{agg}}))^2}{2 (\ln(\sigma_{agg}))^2} \right]. \quad (3)$$

549 The emitted mass fraction of mineral i in different dust modes, arising from clay-sized ($M_{c,i}$) or
 550 other-sized ($M_{o,i}$) soil category, is computed by integrating either Equation 4 for the
 551 accumulation dust mode or Equation 5 for larger dust modes. The integration bounds correspond
 552 to the mode cutoff sizes listed in Table 2:

$$\frac{dM_{d,i}}{d\ln D_d} = M_{c,i} \frac{dM_d}{d\ln D_d} \text{ for } D_d \leq 2 \mu\text{m}, \quad (4)$$

$$\begin{aligned} \frac{dM_{d,i}}{d\ln D_d} = M_{c,i} \frac{dM_d}{d\ln D_d} + M_{o,i} \frac{D_d}{C_m} \left[\operatorname{erf} \left(\frac{\ln(D_d/\overline{D_s})}{\sqrt{2} \ln(\sigma_s)} \right) \right. \\ \left. - \operatorname{erf} \left(\frac{\ln(2/\overline{D_s})}{\sqrt{2} \ln(\sigma_s)} \right) \right] \int_0^\infty \exp \left(-\frac{D_d}{f_\lambda D_{agg}} \right)^3 P_{agg}(D_{agg}) dD_{agg}, \text{ for } 2 \mu\text{m} < D_d \\ \leq 70 \mu\text{m}. \end{aligned} \quad (5)$$

553 3.4 The EMIT Soil Mineralogy Atlas

554 EMIT detects ten soil minerals (illite, kaolinite, smectite, hematite, goethite, calcite, gypsum,
 555 chlorite, dolomite, and vermiculite) using their spectral signatures with an advanced shortwave
 556 and near-infrared imaging spectrometer (Thompson et al., 2024) from its vantage point on the
 557 International Space Station (Green et al., 2020). Mineral identification is conducted at the
 558 instrument's native spatial resolution of 60 meters, employing the Tetracorder linear feature-
 559 matching algorithm (Clark et al., 2024) to interpret surface reflectance. Mass fractions are
 560 subsequently estimated using a Hapke-like radiative transfer model (Hapke, 1981), which
 561 accounts for scattering and reflection within approximately the top centimeter of soil (Clark &
 562 Roush, 1984; Clark et al., 2024), the primary source region for dust emission.

563 To derive size-resolved mineral mass fractions in emitted aerosols, it is necessary to estimate the
 564 distribution of minerals across soil particle sizes. We partition EMIT-derived mineral

abundances into clay ($\leq 2.0 \mu\text{m}$) and silt ($2.0 - 50 \mu\text{m}$) fractions based on established empirical relationships informed by soil texture data, Food and Agriculture Organization (FAO) soil classification maps, and auxiliary constraints, including observed iron oxide concentrations (Perlwitz et al., 2015a) and AERONET-retrieved dust single-scattering albedo (Obiso et al., 2024). Iron oxides are assumed to be uniformly distributed across particle sizes. The resulting mineral mass fractions are allocated to different dust modes following methodologies established in prior work (Gonçalves Ageitos et al., 2023; Perlwitz et al., 2015a) and subsequently applied in our model simulation.

A comprehensive description of the methodology used to generate the mineral atlases is available in previously published documentation (Brodrick, Clark, et al., 2023; Clark et al., 2024; Okin et al., 2023). The publicly released EMIT soil mineral atlases are archived at National Aeronautics and Space Administration (NASA)'s Distributed Active Archive Center (DAAC) (Brodrick, Okin, et al., 2023).

EMIT soil mineralogy used in this study is derived using Tetracorder expert system 5.27c1 (Clark, 2024; Clark et al., 2024), which has known deficiencies, including misidentifying some nano-hematite-nano-goethite mixtures as jarosite. Thus, the total hematite abundance could be under-reported by the EMIT delivery used for this study. The EMIT team is working on a new reflectance model, and this known deficiency has been mitigated in newer versions (Tetracorder expert system 5.27e1 and later) and the EMIT team will recalculate the global mineral starting later in 2025.

The EMIT retrievals are made across latitudes between 60°S and 60°N . We mask areas where there is solid rock (see Section 3.2). High-latitude dust sources exist (Groot Zwaaftink et al., 2016; Meinander et al., 2022). Although their contribution to the global mean annual dust direct radiative effect is minor due to small dust loadings, limited vertical extent, low surface temperatures, and reduced solar irradiance at high latitudes, they can considerably impact regional climates by interacting with clouds (Shi et al., 2021), glaciers, and land or ocean ecosystems (Bullard, 2017). To account for these sources and fill gaps in areas where the EMIT soil atlas provides no data, soil mineralogy from Claquin et al. (1999) is applied.

For our dust model, chlorite, vermiculite, and kaolinite are grouped and collectively transported as kaolinite, using the physical properties of kaolinite. Initial tests indicate that different combinations (e.g., combining chlorite, vermiculite, and illite, and using the physical properties of illite) have a negligible impact on dust direct radiative effect calculations, given the smaller optic differences among them compared to their differences with iron oxides, particularly at the visible band. Similarly, hematite and goethite are combined and treated as iron oxides due to the limited availability and questionable accuracy of refractive indices for goethite (Warren et al., 2019). Constrained refractive indices, which accurately capture the optical properties of dust aerosols in the shortwave spectral range with the combined iron oxides (Li et al., 2024), are applied to the total iron oxide component.

4 Model Configuration

CAM6 with either aerosol model is configured with sea surface temperature prescribed from measurements, with the atmosphere coupled to active land and sea ice models, and to data ocean and slab glacier models. Two simulations (Table 3), both tuned to have almost identical global dust optical depth (0.030) in the visible band, are conducted to quantify the modeled dust cycle, allowing for a thorough evaluation of the new and old dust models and inter-model comparisons. Therefore, one simulation utilizes the new model with all implemented changes introduced in Section 3, while the other uses the old model introduced in Section 2 with observationally constrained optics for simulated iron oxide aerosols. Both simulations are performed at a horizontal spatial resolution of $1.25^\circ \times 0.9^\circ$ (longitude by latitude) with 56 vertical layers up to 2.0 hPa with offline meteorological fields (air temperature, horizontal wind, and relative humidity) taken from the MERRA2 reanalysis data for the period 2006 - 2011 (only the last five-year results are used for data analysis). Anthropogenic emissions are from the Coupled Model Intercomparison Project Phase 6 (CMIP6) inventory for the year 2000 (Eyring et al., 2016).

5 Observational Data for Model Performance Evaluation

5.1 Observations of Dust Aerosol Size Distribution

We utilize previously compiled and harmonized measurements of size distributions (Formenti & Di Biagio, 2024) for freshly emitted dust (residence time less than 1.0 day), as well as dust

following medium (1.0 - 4.0 days), and long (more than 4.0 days) range transport. This classification includes 12, 36, and 10 locations for short-, medium-, and long-range transported dust, respectively.

The compilation comprises 58 datasets collected from literature published over the past 50 years. These datasets were gathered at various locations using different measurement techniques, including microscopy, Coulter multisizers, optical particle counters, optical array probes, and mobility particle sizers. They feature diverse operational size definitions (e.g., optical, projected-area, aerodynamic, and geometric), sampling concentrations and size information (e.g., resolutions and ranges). Such variability complicates accurate and comparable analysis of dust size distributions across sources and transport stages, posing challenges for model evaluation. To address these inconsistencies, Formenti and Di Biagio harmonized the data at four levels (Levels 0, 1, 2a, and 2b). Detailed documentation of the dataset is provided by Formenti and Di Biagio (2024).

This study uses their Level 2b data to evaluate modeled dust size distributions. This dataset is derived through three key steps: (1) interpolating original data from publications over a common size range with equi-logarithmically spaced diameters; (2) renormalizing the interpolated data so that the integral equals unity over a defined diameter range, enabling direct comparison of size distribution shapes rather than absolute values; and (3) harmonizing observed particle diameters by converting them to a common equivalent geometric diameter that accounts for dust asphericity. These procedures ensure a robust and consistent dataset that accounts for inherent differences in dust size distribution measurements, facilitating a better understanding of dust particle size dynamics across different transport stages and a consistent comparison of modeled dust size distribution.

5.2 Dust Optical Depth and Deposition Flux

To evaluate our simulated dust optical depth in the visible band, we compared it against AERONET retrievals (aerosol optical depth Version 2 Direct Sun Algorithm, Level 2.0) at the wavelength of 0.55 μm that were postprocessed by Albani et al. (2014). The postprocessing includes rigorous data quality control procedures and station selection criteria based on the dominance of dust optical depth in the reported total aerosol optical depth (Albani et al., 2014).

The dust deposition flux data utilized in this study were originally compiled by Albani et al. (2014) from various sources (Ginoux et al., 2001; Lawrence & Neff, 2009; Mahowald et al., 2009; Tegen et al., 2002) for present-day climate conditions. Reported mass fractions of dust particles smaller than 10 μm in diameter are used to estimate the total dust deposition flux, including contributions from coarser particles, for comparison with the total flux simulated by both MAM versions.

5.3 Elemental Aluminum Concentration

Elemental aluminum, often found in mineral dust aerosols associated with aluminosilicate, is widely used to identify mineral aerosols within an aerosol population (Formenti et al., 2001; Measures & Vink, 2000; Prospero et al., 2001). We compare elemental aluminum particulate matter derived from simulated minerals with aerodynamic diameters of up to 2.5 μm ($\text{PM}_{2.5}$) and 10 μm (PM_{10}) to newly compiled data from Mahowald et al. (2024). This dataset synthesizes a wide range of mass measurements for $\text{PM}_{2.5}$ and PM_{10} aerosol particles from the literature and public health databases.

The cutoff size at 2.5 μm or 10 μm is established according to aerodynamic diameter guidelines, which inform inlet design in reference methods. These $\text{PM}_{2.5}$ and PM_{10} values correspond to $\text{PM}_{1.6}$ and $\text{PM}_{6.9}$, respectively, in geometric space, which defines the aerosol sizes in our model. We considered this difference in size concept when preparing the model results for comparison, following Reid et al. (2003), using a dynamic shape factor of approximately 1.5.

5.4 Mineral Aerosol

We assess modeled mineral fractions in surface concentrations and deposition fluxes using data previously compiled at 154 locations (Perlwitz et al., 2015a, 2015b), with dust primarily transported from North Africa, the Middle East, and Asia. This dataset includes observations from individual points and averages along ship tracks, with sampling periods ranging from single days to several years, spanning the late 1960s to the 2000s. For details on sample numbers, standard deviations, sampling periods, size ranges, locations, and vessel tracks, see Perlwitz et al. (2015) and references therein. Although most studies in the compilation aimed to measure mineral fractions from dust aerosols (e.g., by extracting dust with polycarbonate or quartz

microfibers, cellulose filters, or other filters, or by selecting dust-heavy episodes), various sources of error still exist, which may affect the interpretation of the model-data comparison.

To evaluate the model's ability to simulate dust mineral composition, we compare model results with observed minerals filtered by Gonçalves Ageitos et al. (2023) to exclude potential anthropogenic contamination by aerosols from industrial activities and combustion processes (Chen et al., 2012; Luo et al., 2008). Observed minerals are mapped to model components, recalibrating mass fractions and standard deviations to account for unrepresented species (e.g., grouping all iron oxides as hematite). The interannual variability of mineral fractions is considered low, enabling comparison between observed values and modeled multi-annual means (Perlwitz et al., 2015a). Model outputs are matched to observations in time (monthly climatology), space, and size by collocating resolved size distributions at corresponding locations and times. For MAM4, only observations with particle sizes smaller than 10 μm in diameter are retained, while broader size ranges are used for MAM10 following Gonçalves Ageitos et al. (2023). Here, we additionally include model-observation comparisons for dust particles larger than 20 μm . Text S4 in Supporting Information describes in detail how the mineral fraction dataset is used.

EMIT provides total mineral abundances in soils but does not resolve their size distribution. It also does not directly retrieve quartz and feldspar. The first version of the EMIT-derived soil map for use in mineral-resolved models, including this study, incorporates pre-EMIT soil mineral atlases and empirical relationships that rely on soil texture data to describe the partitioning of quartz and feldspar, as well as the size distribution of calcite. In order to minimize the impact of these assumptions on model-observation comparisons, we group quartz, feldspar, and calcite simulated by MAM10 into a single category for comparison with observations.

6 Statistical Metrics and Limitations in Model-Observation Comparison

We assess model performance in simulating dust mineralogy by comparing modeled and observed mineral composition (e.g., ratios of minerals both modeled and observed) and size distribution at corresponding locations and times, using monthly climatology. The modeled dust size distribution is evaluated using monthly climatology, whereas comparisons involving elemental aluminum, dust optical depth, and total dust deposition flux are based on annual

means, except when assessing their seasonal cycles, which are evaluated on a monthly basis. For most model-observation pairs, we compute (normalized) mean bias, (normalized) root mean square error, or Pearson correlation coefficients in space or time. Statistical significance of the correlations is tested at the 95% confidence level.

Although model outputs are selected to align as closely as possible in both space and time with available measurements, several potential limitations in the model-observation comparison remain and may affect the interpretation of results, as previously summarized (Li et al., 2022). These limitations include the following aspects:

First, temporal mismatch. Observational campaigns often span only a few days to weeks, while model results are reported as monthly means. Although we compare monthly climatology, this discrepancy may introduce uncertainties, particularly given the episodic nature of dust events. The short duration of measurements may not reliably represent climatological conditions, and this mismatch is a common issue across all model-observation comparisons presented in this study. We do not quantify the uncertainty introduced by this limitation.

Second, differences in spatial representativeness. Model outputs reflect averages over grid cells that can span hundreds of kilometers, whereas observational data, such as those from ground stations or aircraft, capture dust properties at much finer spatial scales. This difference in spatial sampling volumes can lead to discrepancies, particularly in regions with strong spatial gradients in dust concentration.

Third, potential bias in data site selection. Some AERONET site selections are based on modeled aerosol fields, which may not accurately reflect actual optical depth conditions for both dust and non-dust aerosols. This introduces potential bias into the validation process.

Fourth, observational uncertainties. Observational datasets themselves are subject to errors. For example, AERONET aerosol optical depth retrievals may be affected by cloud-screening algorithms (Levy et al., 2010), and postprocessing procedures applied to dust size distribution data from different field campaigns (Section 5.1) can introduce additional uncertainties (Formenti & Di Biagio, 2024).

Fifth, inconsistencies in mineral types between the model and observations, as well as

differences in the number of observation points used for MAM4 and MAM10. Modeled mineral fractions are collocated with observations in time (monthly climatology), space (nearest model grid cell), size, and mineral composition. For the compositional comparison, only minerals present in both the model and observations at a given site are considered, with uncommon minerals excluded rather than dropping the site entirely. This approach maximizes the number of usable observational points per mineral, as not all sites report all modeled minerals. However, it introduces discrepancies in relative mass fractions at sites where the set of modeled minerals differs, for example, between pre-EMIT (Claquin et al., 1999) and EMIT-based simulations, where chlorite, vermiculite, and kaolinite are grouped and collectively simulated as kaolinite. Additionally, the distinct size ranges represented by MAM4 and MAM10 result in different subsets of valid observational data for each model. As a result, the statistical metrics reflect not only differences in model performance for comparable size ranges but also artifacts introduced by these inconsistencies, complicating direct comparisons between MAM4 and MAM10 in reproducing observed mineral mass fractions.

7 Results

7.1 Simulated Global Annual Dust Budget Climatology

With a globally averaged dust optical depth of approximately 0.030 in the visible band (0.44 - 0.63 μm) following the dust model tuning (Table 3), the inclusion of dust particles larger than 10 μm in diameter increases the simulated annual global dust budget. During the 2007 - 2011 period, the MAM10 model simulates higher dust emission, deposition fluxes (9500 versus 2900 Tg year^{-1}), and loadings (40 versus 24 Tg) compared to MAM4. The inclusion of super coarse and giant dust particles enhances dry deposition more than wet deposition, increasing the dry-to-wet deposition ratio. This disparity primarily results from the stronger gravitational settling of coarser dust particles, whose deposition predominantly occurs in arid regions with low precipitation (see Section 7.3). Table 4 provides further details on the distribution of simulated global dust quantities across different size modes.

The disproportionately large deposition (or emission) relative to loadings in MAM10, compared to MAM4, is primarily due to the short lifetime of super coarse (1.1 days) and super coarse/giant dust particles (0.33 days) (i.e., due to differences in particle size distribution). This shorter

lifetime of large particles, combined with the reduced sensitivity of visible-band dust optical depth to large particles because of their low mass extinction efficiency (e.g., A5: $2.0 \text{ m}^2 \text{ g}^{-1}$ versus A10: $0.041 \text{ m}^2 \text{ g}^{-1}$; and MAM10: $0.40 \text{ m}^2 \text{ g}^{-1}$ versus MAM4: $1.3 \text{ m}^2 \text{ g}^{-1}$), and dust tuning toward a global mean visible-band dust optical depth of 0.030 (Tables 3 and 4) collectively explains why MAM10, despite simulating substantial increases in the dust loading and emission, maintains a global mean visible-band dust optical depth comparable to MAM4.

Particularly, our diagnosed dust quantities for a cutoff size of $10 \text{ }\mu\text{m}$ in diameter, based on the simulated size distribution of aged dust, suggest that the higher dust loadings in MAM10 compared to MAM4 primarily result from dust particles between 2.0 and $10 \text{ }\mu\text{m}$. Dust particles larger than $10 \text{ }\mu\text{m}$ account for 10 Tg (25% of total dust loading), while dust smaller than $10 \text{ }\mu\text{m}$ accounts for 30 Tg (75% of total dust loading) in MAM10, which is 25% higher than in MAM4. The high loading within the $2.0 - 10 \text{ }\mu\text{m}$ geometric diameter range, which may partially explain the overestimated surface elemental aluminum with aerodynamic diameters between 2.5 and $10 \text{ }\mu\text{m}$ (see Section 7.2.1), primarily results from the reduced simulated settling velocity of medium-coarse dust particles in MAM10 (Table 3). This high loading in the $2.0 - 10 \text{ }\mu\text{m}$ geometric diameter range, accompanied by a slight compensatory reduction in absolute dust mass for particles smaller than $2.0 \text{ }\mu\text{m}$, mainly reflects the reduced mass extinction efficiency of dust aerosol in this size range in MAM10. The reduced efficiency, in turn, arises from the model's size distribution parameters for both emitted and transported dust, which are shifted toward coarser particles, thereby lowering visible-band extinction relative to MAM4. As a result, MAM10 requires a higher dust emission rate (implemented through a lower dust emission tuning factor, which is inversely related to the emission rate; Table 3) to maintain the global mean visible-band dust optical depth at approximately 0.030.

792 **Table 4.** *Simulated Global Annual Mean Dust Quantities (years: 2007 - 2011).*

Mode Information	Total; < 10; < 20 μm	A5 (Fine)	A7 (Fine/Coarse)	A8 (Medium Coarse)	A9 (Super Coarse)	A10 (Super Coarse/Giant)
Emission/Deposition (Tg year ⁻¹)	9500; 3100 (33% of total); 5400 (57% of total)	100	1400	1600	2300	4100
Loadings (Tg)	40; 30 (75% of total); 36 (90% of total)	1.9	14	13	7.0	3.5
Lifetime (days)	1.5	11	3.6	2.9	1.1	0.32
Optical Depth in the Visible Band (0.44 - 0.63 μm)	0.031	0.0073	0.016	0.0072	0.0012	0.00028
Visible-Band Mass Extinction Efficiency (m ² g ⁻¹)	0.40	2.0	0.58	0.28	0.087	0.041

793 *Note.* In the second column from the left, numbers in parentheses, if present, indicate the global
794 percentage contribution of dust larger than 10 or 20 μm in diameter to size-integrated dust
795 budgets.

796 We also compare the simulated dust quantities with the inverse modeling results of Kok et al.
797 (2021) for dust diameters smaller than 20 μm . MAM10 simulates a global mean dust emission of
798 5400 Tg year⁻¹ for particles smaller than 20 μm in diameter, which falls within the broad range
799 of 3400 - 9100 Tg year⁻¹ estimated by Kok et al. (2021). However, the simulated dust loading
800 (36 Tg) is 20% higher than the upper range of 22 - 30 Tg reported by Kok et al. (2021). This
801 indicates that MAM10 probably overestimates the amount of dust particles smaller than 20 μm
802 in diameter, despite its simulated size distribution comparing well with observations (see Section
803 7.2.3). To match the dust mass within that size range, tuning the global dust optical depth in the
804 visible band from 0.031 to 0.025, which still falls within the observational range of 0.025 - 0.035
805 (Ridley et al., 2016), might be a good practice if the mass extinction efficiency and dust size
806 distribution remain unchanged.

We did not apply the adjustment in the global dust optical depth for the present study for two primary reasons. First, simulated dust mass is not the focus but rather one of several dust-related quantities we aim to represent reasonably. Second, this adjustment reflects a pragmatic compromise, as the dust optical depth is more directly constrained by observations than dust loading, which is inferred indirectly. As the model-observation agreement on the dust size distribution can still be improved, another possible approach is to further refine the dust size distribution and gravitational settling velocity, which might help reduce the likely overestimation of dust mass compared to Kok et al. (2021). Moreover, the probable underestimation of the impact of dust particle asphericity on mass extinction efficiency may partially explain the overprediction of dust particles smaller than 20 μm by MAM10 relative to Kok et al. (2021).

7.2 Model-Observation Comparison

7.2.1 Annual Mean Dust Cycle Climatology

The new MAM10 reproduces observed dust cycle within an order of magnitude at most sites while maintaining the MAM4 model's accuracy for dust particles smaller than 10 μm in diameter (Figure 1). The incorporation of super coarse and giant dust particles, along with substantially improved dust emission physics and size distribution (see Section 7.2.3), provides limited improvement in capturing the overall climatology of dust optical depth and deposition fluxes.

Across different regions, the combined changes to CAM6 result in varying degrees of accuracy in reproducing the observed dust cycle compared to the earlier version. Simulated dust deposition aligns more closely with observations in some regions (e.g., the South Pacific) but shows larger discrepancies in others (e.g., North Indian). At high latitudes, while suffering from limited data for comparison, both new and old models likely systematically overestimate dust deposition fluxes. This overestimation, which exceeds a factor of two, does not occur in low-to-middle latitude regions. Given the low dust emissions at high latitudes, particularly in the Southern Hemisphere, this discrepancy suggests that the new model, like MAM4, may transport dust from low-latitude source regions likely too efficiently to high latitudes. Consequently, the underestimation of surface dust concentrations and overestimation of deposition observed at several locations, such as near El Djouf and the Antarctic that are present in MAM4 (Li et al.,

2022) and earlier versions of CAM (BAM in CAM4 and MAM3 in CAM5) (Albani et al., 2014), are still evident in MAM10. This phenomenon remains particularly evident at sites like King George in the Antarctic (62° S, 58° W) compared to that in MAM4 (Li et al., 2022), where previous studies using observations combined with multiple model ensembles, including an earlier version of CAM4, have reported similar findings (Kok, et al., 2021).

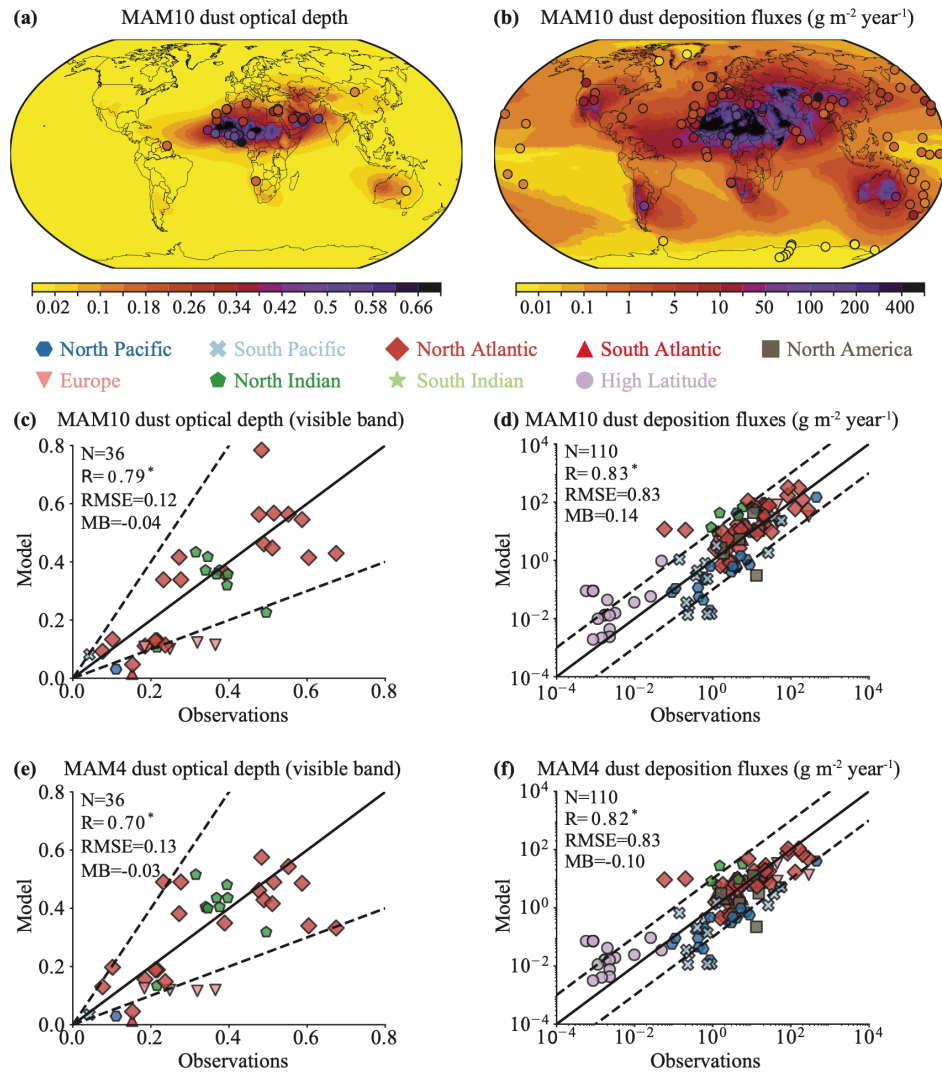


Figure 1. Comparison of simulated total dust quantities with observational data (total number: N) previously compiled (Albani et al., 2014). Panels (a), (c), and (e) show dust optical depth in the 0.44 - 0.63 μm band, while panels (b), (d), and (f) present deposition fluxes. The deposition fluxes represent values across all size ranges. Black solid lines in scatter plots indicate the one-one line, while dashed lines show a factor of 2.0 (panels c and e) or 10 (panels d and f)

847 difference. Model (MAM10: panels a - d; MAM4: panels e and f) performance metrics include
848 Pearson's correlation (R; "*" indicates significance at the 95% confidence level), root mean
849 square error (RMSE), and mean bias (MB), calculated in the logarithmic space for deposition
850 fluxes and in the normal space for dust optical depth.

851 The new model achieves considerable improvements in representing the spatial variation of
852 surface elemental aluminum with aerodynamic diameters smaller than 2.5 μm (Figure 2).
853 However, it almost systematically overestimates that for aerodynamic diameters smaller than 10
854 μm (Figure 3), more specifically between 2.5 and 10 μm , indicating a probable overestimation of
855 emissions for particles in that size range in the model. The cause of this overestimation is
856 unclear. If the model-data comparison for diameters smaller than 2.5 μm and both data are
857 reliable, a probable explanation could be insufficient vertical transport of dust likely due to the
858 process split issue (Wan et al., 2024) in the model (dust dry deposition is applied immediately
859 after emission and then turbulence mixing), which tends to cause dust to unduly accumulate in
860 the bottom model layer. The likely overestimation of dust mass between 2.0 and 10 μm in
861 geometric diameter, as inferred in Section 7.1 compared to Kok et al. (2021), may also partially
862 explain this overestimation.

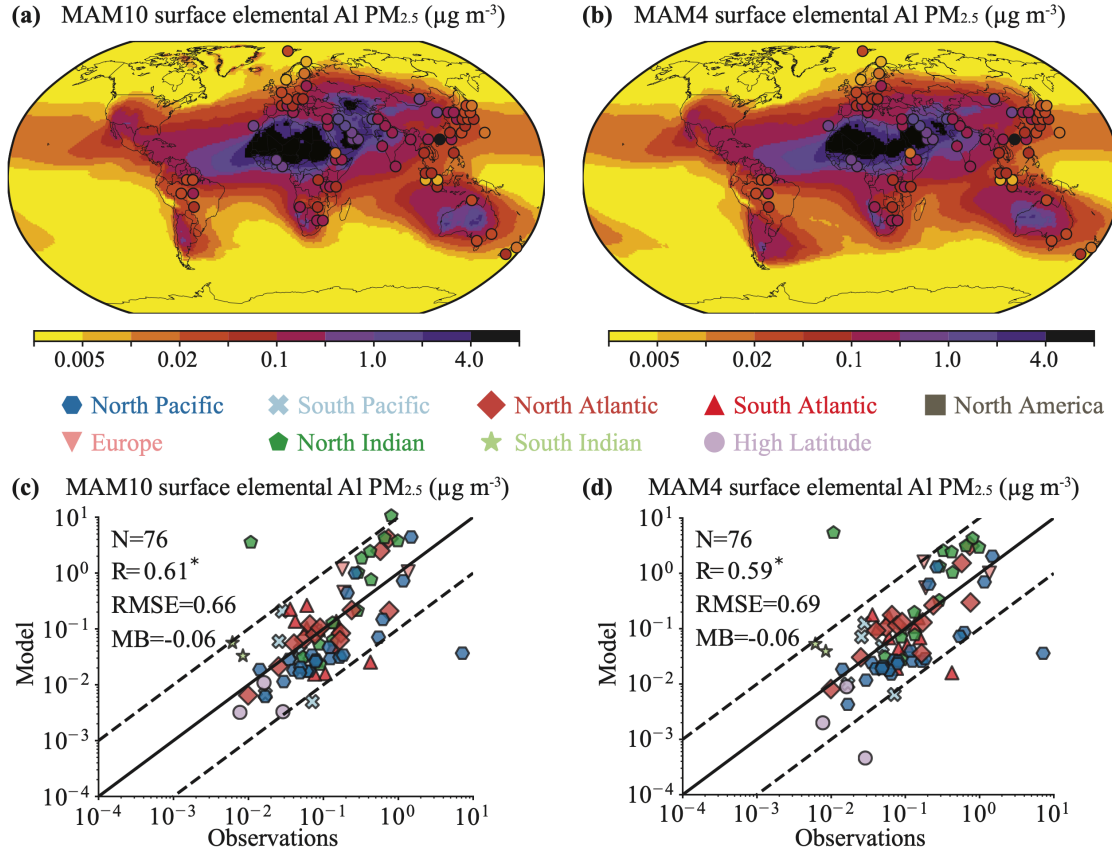


Figure 2. Derived surface elemental aluminum (Al) concentrations based on simulated minerals compared to observations (total number: N) previously compiled (Mahowald et al., 2024) with aerodynamic diameters smaller than $2.5 \mu\text{m}$ (particular matter: PM_{2.5}). Panels (a) and (c) correspond to MAM10, and panels (b) and (d) to MAM4. Observational data were remapped onto a $4^\circ \times 4^\circ$ regular grid, reducing the dataset to 76 points for better visualization and model-data comparison. Model performance metrics include Pearson's correlation (R ; "*" indicates significance at the 95% confidence level), root mean square error (RMSE), and mean bias (MB), calculated in the logarithmic space.

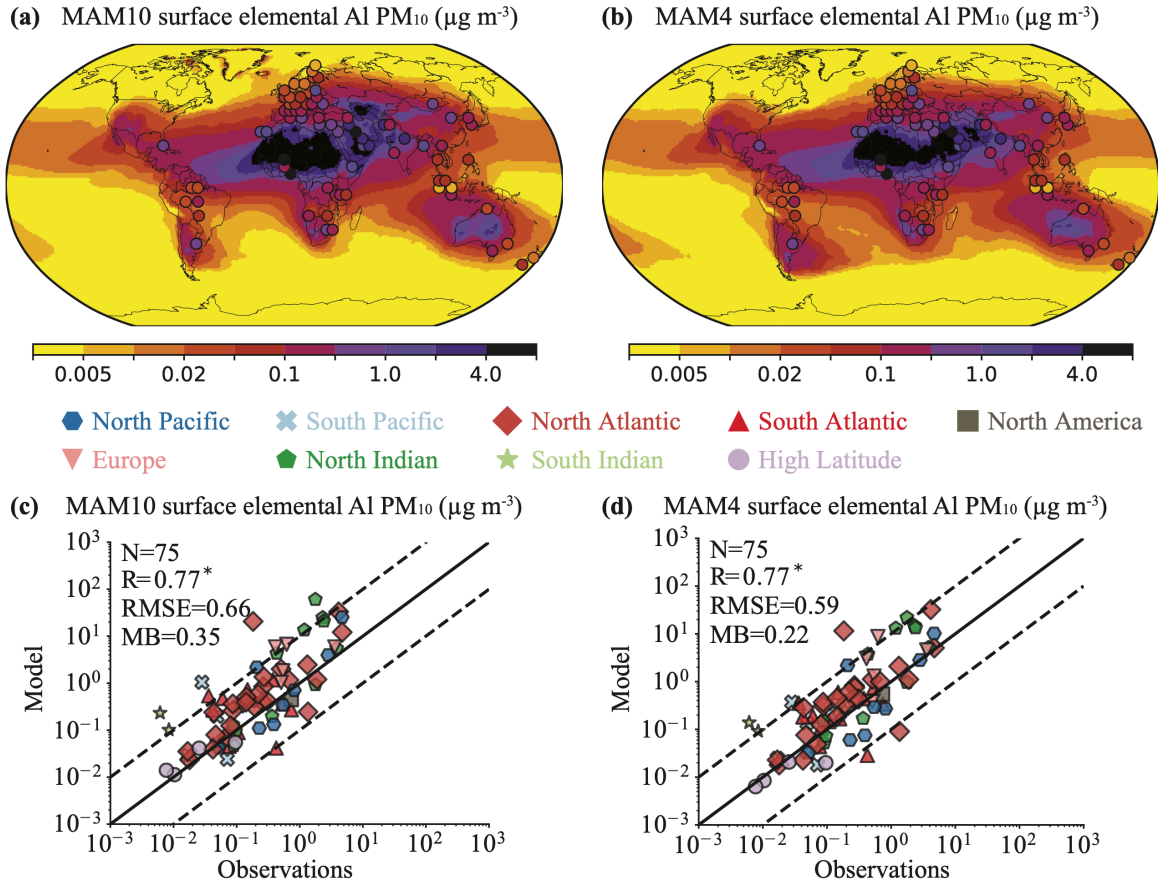


Figure 3. Derived surface elemental aluminum (Al) concentrations based on simulated minerals compared to observations (total number: N) previously compiled (Mahowald et al., 2024). Same as Figure 2 but with aerodynamic diameters smaller than $10\ \mu\text{m}$ (particulate matter: PM_{10}).

The persistent discrepancies between modeling and observations highlight uncertainty in modeling the dust cycle and in model-data comparisons, influenced by multiple factors summarized in Section 6 and by a previous study (Li et al., 2022), for which we still lack sufficient information to address. Here, we highlight two additional factors beyond.

First, a known yet unquantifiable error source stems from sparse station-based measurements available for model-data comparison, particularly in dust source regions. This limitation biases dust aerosol emission modeling, likely leading to overestimated emissions over North Africa (Li et al., 2022), which remains evident in MAM10, due to the global tuning to achieve a mean dust optical depth of approximately 0.030. Thus, regional refinement of dust emission might be necessary.

Second, the available measurements themselves are subject to uncertainty, such as those related to deposition (Mahowald et al., 2005) and surface elemental aluminum concentrations (Mahowald et al., 2025). Post-processing procedures applied to reported measurements by original studies likely introduce further uncertainties, as noted for dust size distribution harmonization (Formenti & Di Biagio, 2024).

7.2.2 Seasonality of Dust Aerosol

Given the importance of simulating dust seasonality, which interacts with other Earth system components like ocean and land biogeochemistry, we assess the model's ability to reproduce dust seasonality in Figure 4 using previously compiled climatologically monthly mean data for AERONET dust optical depth at the 0.55 μm and surface concentrations (Albani et al., 2014).

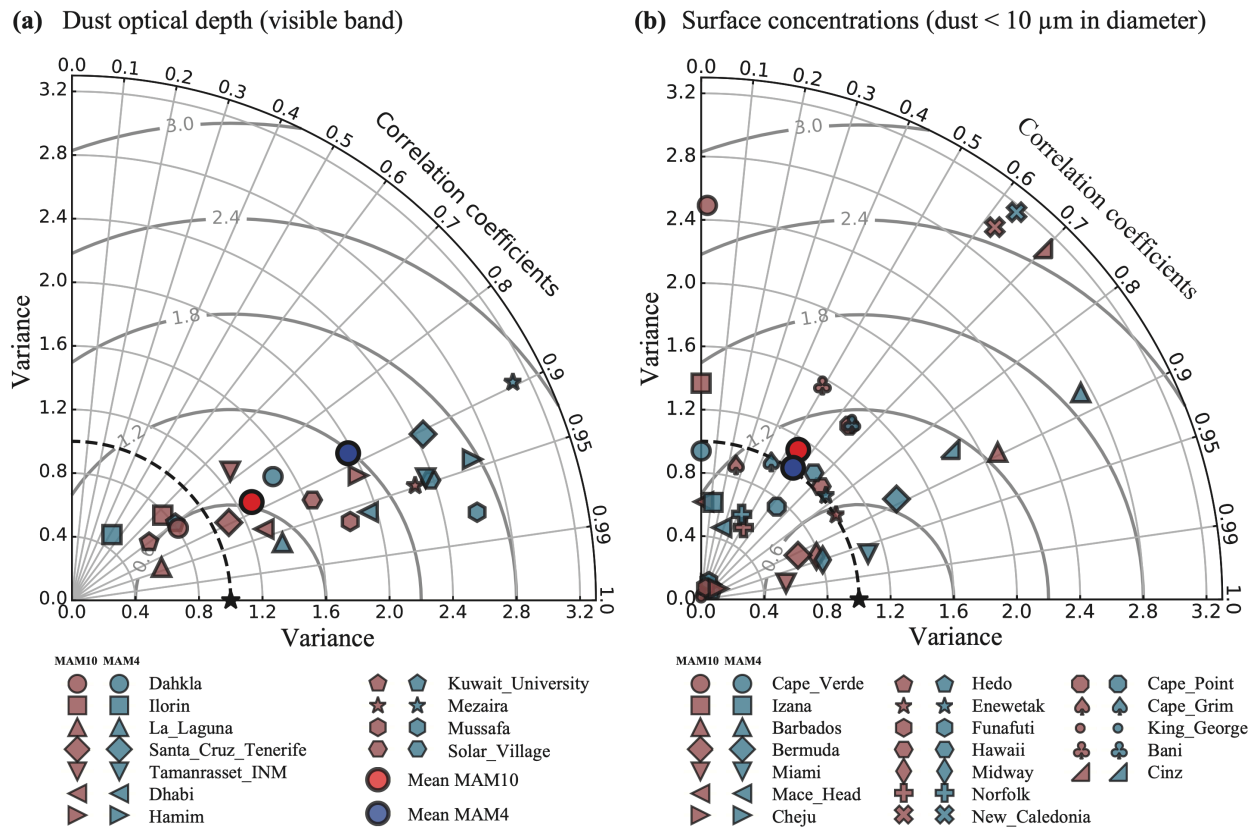


Figure 4. Model-data comparison of dust seasonality, defined as the monthly mean climatology. Panel (a) shows results obtained for dust optical depth, while panel (b) presents surface dust concentrations with the geometric diameter smaller than 10 μm . Seasonal data compiled by Albani et al. (2014) were used to evaluate the model's performance.

MAM10 simulates different seasonal cycle amplitudes of dust optical depth in the visible band (Figure 4a) and surface concentrations (Figure 4b) from MAM4, although the temporal correlations are similar between the two models, better for dust optical depth than for the surface concentrations. Overall, the new model slightly improves the simulated seasonal amplitude of the visible-band dust optical depth (Figure 4a), while slightly degrading that for the surface concentrations (Figure 4b). This improvement is primarily attributed to the inclusion of drag partitioning in the updated dust emission scheme (Leung et al., 2023), which reduces dust emission during peak summer while having a minimal effect in winter (Leung et al., 2024). The different performance on the dust optical depth in the visible band and surface concentrations is not paradoxical, as the observations were made at different locations. The two variables also differ: dust optical depth is a column-integrated variable, whereas surface concentration represents only the bottom model level and depends on the accuracy of simulated vertical dust transport. Because of this difference, another possible explanation for the different behavior in the dust optical depth versus surface concentration is that the model's vertical mixing of dust aerosols is likely insufficient, as discussed in Section 7.2.1, and has a seasonal cycle that is also not well simulated. Determining the “true” cause requires further investigation, which is beyond the scope of this study.

7.2.3 Dust Size Distribution

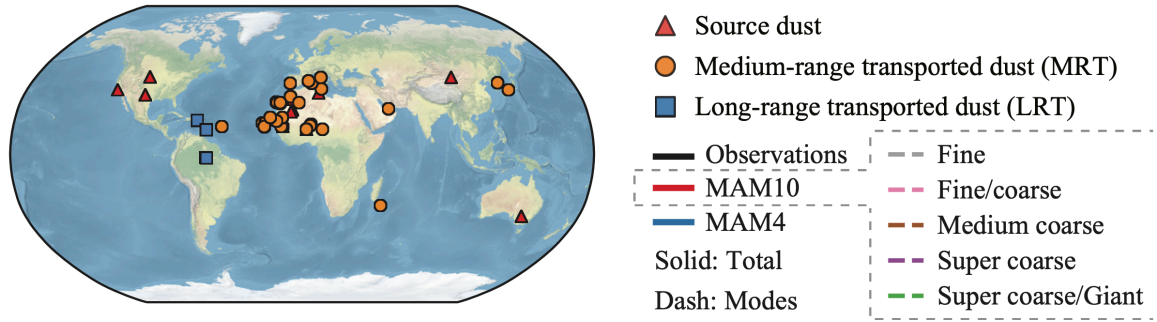
Monthly dust size distributions are calculated offline using simulated monthly mass mixing ratios and number concentrations of different aerosol species in each dust mode, the prescribed geometric standard deviation, and the air temperature and pressure near the atmospheric levels where dust size measurements were taken. Using the calculated monthly values at locations near the measurement sites, the climatological dust size distribution is then derived and compared with observations.

Three things are worth noting before interpreting the model-observation comparisons. First, there is a non-linear relationship between the dust size distribution and the variables used in the calculations. As a result, using monthly modeled values to compute the monthly dust size distribution may introduce uncertainties, compared to performing the calculations at each model time step and then averaging over a month. Second, the size distribution measurements for dust

930 between 0.40 and 10 μm are more reliable due to the higher data volume within this range
931 (Formenti & Di Biagio, 2024) compared to outside this range, where measuring dust becomes
932 more challenging. Third, in addition to uncertainties introduced during postprocessing (Formenti
933 & Di Biagio, 2024), this dataset and the model-data comparison may face similar shortcomings
934 discussed for the other datasets (Section 6).

935 Despite any shortcomings in the observations and model-observation comparison, the size
936 settings and reduced settling velocities applied to the last three dust modes in MAM10 provide a
937 significantly better representation of observed dust size distributions compared to MAM4, which
938 simulates almost no dust particles larger than 10 μm (Figure 5). The simulated dust size
939 distribution in MAM10 is within observational uncertainties across most size ranges, except for
940 medium-range transported dust coarser than 50 μm , which the new mode underestimates (though
941 not significantly), and particles smaller than 0.40 μm , which both models overestimate. MAM10
942 simulates a clear size dynamic, where the two largest dust modes gradually disappear during
943 transport, while the fine modes remain largely unchanged, which is consistent with observations
944 (Formenti & Di Biagio, 2024). In contrast, MAM4 shows little change in its single coarse mode
945 across varying distances from the source regions.

(a) Geographical location of the observations



(b) Volume distribution of dust aerosols

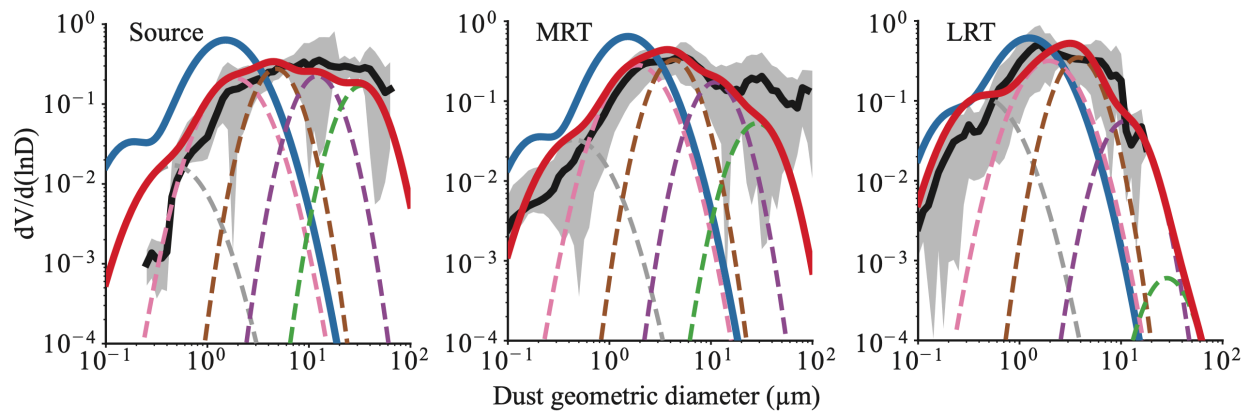


Figure 5. Modeled dust volume size distributions compared to observations previously compiled (Formenti & Di Biagio, 2024). Panel (a) indicates observation locations for the size-resolved data, while panel (b) compares modeled and observed size distribution for dust categorized by transport distance from source regions for MAM10 (red solid lines and dash lines for individual dust modes) and MAM4 (blue solid lines). Model results corresponding to the atmospheric levels, locations, and months of observations were used. Both modeled and observed data are normalized for dust particles across the full-size ranges. The five dust modes correspond to distinct size ranges of emitted particles: Fine (0.10 - 1.0 μm), fine/coarse (1.0 - 5.0 μm), medium coarse (5.0 - 10 μm), super coarse (10 - 20 μm), and super coarse/giant (20 - 70 μm).

The new model's performance is improved by incorporating new dust modes that represent super coarse and giant dust and applying reductions in their gravitational settling velocity: 85% for the giant dust mode and 75% for the super coarse dust mode. We also reduce 50% of the simulated gravitational settling velocity for the medium-coarse dust mode. These reductions are generally comparable to the approximately 45 - 60% reductions for particles 10 - 30 μm in the Georgia Institute of Technology Goddard model (Ginoux, 2003), though lower than the 80 and 90%

reductions applied in Weather Research and Forecasting (WRF) (Drakaki et al., 2022) and CAM-BAM (Meng et al., 2022), respectively. This reduction amplitude difference could reflect structural (e.g., model resolution) and parametric (e.g., drag coefficients) variations across models.

In MAM10, giant dust particles still likely settle too quickly during medium-range transport, while observations suggest invariant dynamics for dust above 10 μm , or dust fails to be sufficiently uplifted to reach the measurement altitude. A greater reduction in settling velocity is avoided to prevent overestimating the fraction of dust coarser than 20 μm over source regions. It is worth noting again the uncertainties in the observations and the model-observation comparison approach, which may complicate the interpretation of the results. For example, the unknown processes (see Section 8) may systematically reduce the settling velocity of super coarse and giant dust particles only under specific atmospheric conditions that occur during the field campaigns and do not occur elsewhere. Because modeled climatological mean dust size distributions are compared with measurements from field campaigns that typically last only a few days (Formenti & Di Biagio, 2024) and are therefore more representative of specific events than the models' climatological means, this time mismatch could probably introduce uncertainties in the model-observation comparison, particularly for medium- and long-range transported dust.

7.2.4 Mineral Aerosol

As described in Section 3, the new MAM10 integrates several recent advancements, including: (1) a revised dust aerosol size distribution, (2) an extended brittle fragmentation theory that enables the emission of super coarse and giant dust particles, (3) an improved EMIT-derived soil mineral atlas, and (4) modified iron oxide content in the three largest dust size modes through updates to the EMIT soil mineral atlas. This study does not attempt a systematic comparison between simulations using the EMIT and pre-EMIT soil mineral atlases, which will be the focus of a forthcoming publication. Nor do we isolate the contribution of each individual development. Instead, our focus is on evaluating the overall performance of the new model, incorporating these combined developments, in reproducing observed mineral fractions in surface concentrations, dry deposition, and total deposition.

991 Simulations conducted with and without these modifications exhibit similar spatial distributions
992 of mineral mass fractions. However, the combined developments increase the abundance of
993 kaolinite relative to the other minerals (Figure S1 in Supporting Information), primarily at the
994 expense of smectite (Figure S1 in Supporting Information) and quartz (Figure S2 in Supporting
995 Information), as well as iron oxides (Figure 6) and gypsum (Figure S3 in Supporting
996 Information), both at the global scale and across the majority of grid cells.

997 A direct comparison between the new and old models using observed mineral mass fractions is
998 not feasible, as the metrics presented in the paired subpanels of Figures 7 and S4 in Supporting
999 Information correspond to different particle size categories and numbers of observation points.
1000 Despite this limitation, the new model successfully simulates mineral fractions in dust aerosol
1001 particles larger than 10 or 20 μm in diameter, which are not represented in the old model. The
1002 extension of mineral size representation alone marks a substantial advancement of the new
1003 model over the old one. The existing discrepancies between the modeled and observed minerals
1004 do not necessarily reflect limitations in the EMIT surface mineralogy retrievals (see Section 8).

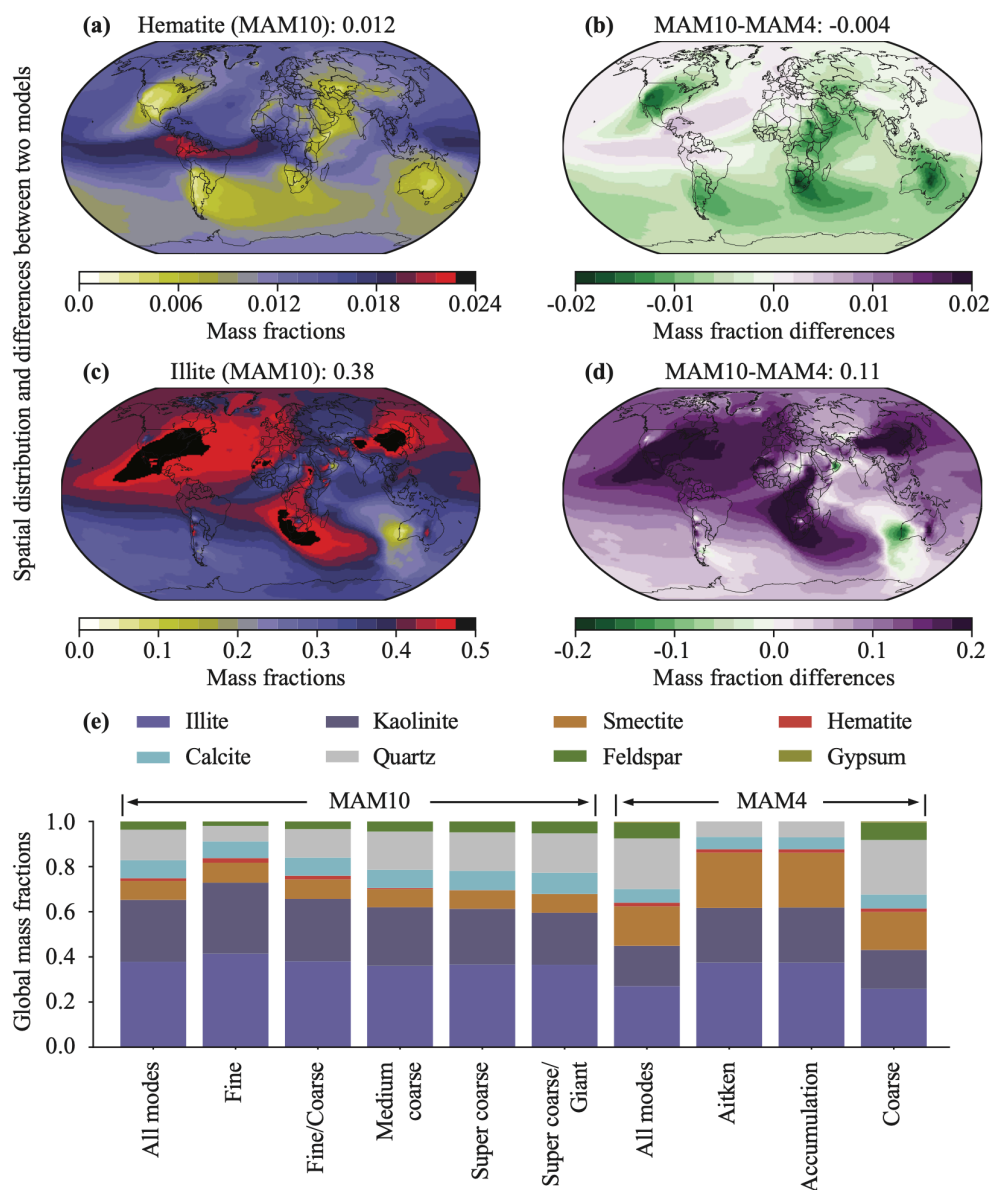
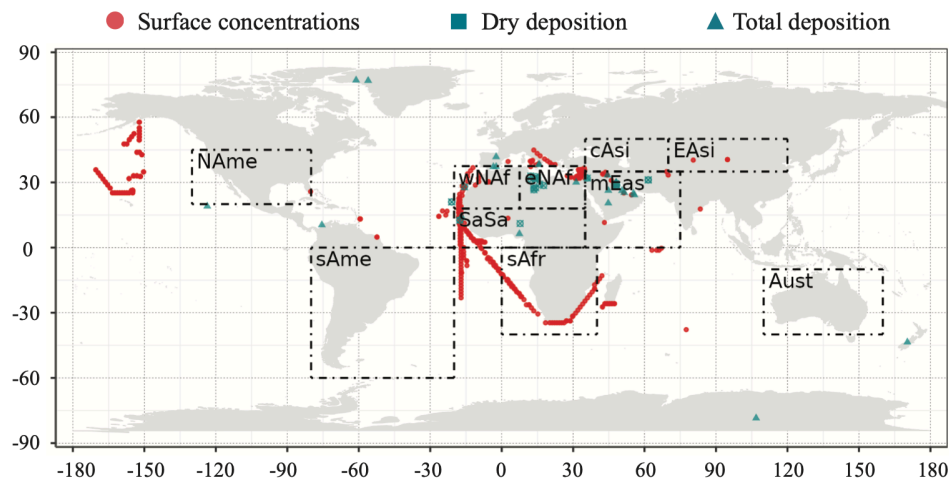


Figure 6. Simulated mineral mass fractions. Panels (a) - (d) show the spatial distribution of simulated hematite and illite, as well as their differences between MAM10 and MAM4. Panel (e) presents the global mean mass fractions of simulated minerals by MAM10 and MAM4 in different size ranges.

(a) Geographic locations of mineral samples



(b) Comparisons

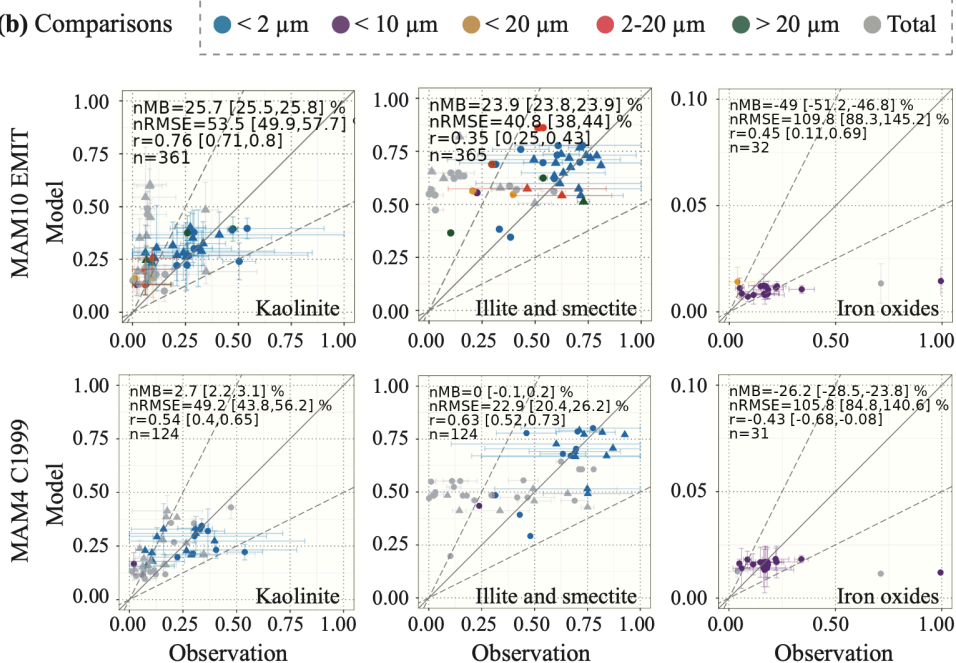


Figure 7. Mineral sample locations and model-simulated mineral fraction in surface concentrations or depositions compared to previously compiled observations (total number: n) (Perlwitz et al., 2015) using the approach of Gonçalves Ageitos et al. (2023). (a) Mineral sample locations categorized by geophysical zones, obtained from surface concentrations (red circles), dry deposition (green squares), or total deposition (green triangles). (b) Model-data comparisons for kaolinite, smectite, and iron oxides across different size (geometric diameter) segments: top panels for MAM10 with the EMIT soil atlas and bottom panels for MAM4 with the Claquin et al. (1999) soil atlas (C1999). Model performance is evaluated using normalized mean bias

(nMB), normalized root mean square error (nRMSE), and size and spatial correlation (r), based on different sample sizes (n : number of observational samples used in each plot). See Figure S4 in Supporting Information for the other minerals.

Overall, the new model shows improved capability but still faces challenges in reproducing both the observed magnitude and spatial variability of mineral mass fractions (Figures 7 and S4 in Supporting Information). It captures the mass fraction of kaolinite, the combined fraction of illite and smectite (Figure 7), and the combined fraction of quartz, feldspar, and calcite (Figure S4 in Supporting Information) within a factor of two at many sites and across multiple size categories. Furthermore, it reproduces the observed spatial distribution of several minerals, including iron oxides with a moderate correlation of 0.45 with measured mass fractions (Figure 7).

Limited observations at sparse locations also indicate size-dependent variations in aerosol mineral composition. For example, the mass fraction of iron oxides tends to decrease with increasing particle size (Kandler et al., 2009; Panta et al., 2023). This trend is captured, to some extent, by the combined modifications (Figure 6). MAM10 simulates highly uncertain mass fractions of iron oxides in the last two dust modes, due to the lack of robust observational constraints on the abundance of iron oxides in giant dust particles. While some studies report almost zero iron oxides in giant dust particles (Kandler et al., 2009; Panta et al., 2023), this reflects an underestimation by electron microscopy, which identifies iron oxides in isolated particles but not in inclusions, rather than their actual absence.

7.3 Improved Representation of Size-Resolved Dust Quantities

Dust aerosols of different sizes/modes exhibit varying physical properties, meaning the modeled dust quantities and their distribution among modes are sensitive to changes in size and mode number. Figure 8a addresses how the new model improves the relative distribution of dust quantities, including the optical depth, deposition, loadings, or $PM_{2.5}$ globally, compared to MAM4.

In MAM4, a single coarse mode constitutes 80% (Figure 8a) of the total dust optical depth in the visible band centered at $0.53\ \mu\text{m}$, which fails to capture the diverse scattering and absorption behaviors of dust particles of different sizes. The increased number of dust modes in MAM10

addresses this limitation by distributing 70% of the global dust optical depth across the first two smallest dust modes (fine and fine/coarse), with the fine/coarse mode being the primary contributor (50%; Figure 8a). Among the medium coarse, super coarse, and super coarse/giant dust modes, the dust optical depth is more evenly distributed, with each mode contributing minimally. This reduced contribution primarily arises from lower mass or volume extinction efficiencies and the preferential removal of coarse and giant dust particles by size-dependent aerosol removal mechanisms, such as gravitational settling.

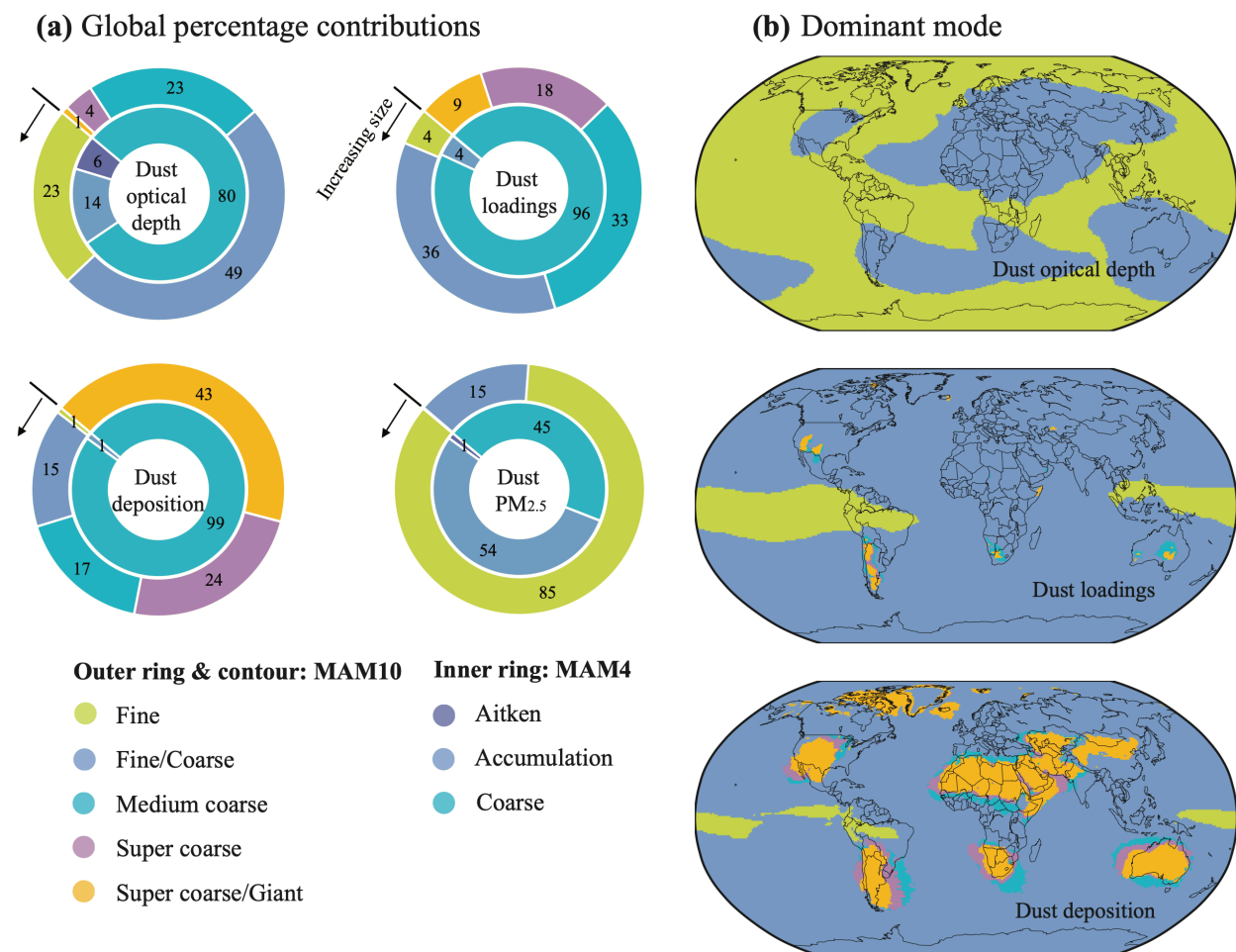


Figure 8. Simulated percentage contribution of individual dust modes to various dust quantities (panel a; MAM10: outer ring; MAM4: inner ring) and spatial distribution of the dominant dust mode in MAM10 (panel b). The dominant mode is the dust mode that contributes the most to a given dust quantity among the five (three) dust modes in MAM10(4). The dust quantities include: (1) visible-band dust optical depth (top-left rings in panel a and top map in panel b), (2) column-integrated dust mass (top-right rings in panel a and middle map in panel b), (3) total (dry

+ wet) dust deposition (bottom-left rings in panel a and bottom map in panel b), and (4) surface particular matter concentrations (bottom-right rings in panel a) with aerodynamic diameters smaller than $2.5\ \mu\text{m}$ ($\text{PM}_{2.5}$). The five dust modes in MAM10 cover size ranges of $0.10 - 1.0$ (fine), $1.0 - 5.0$ (fine/coarse), $5.0 - 10$ (medium coarse), $10 - 20$ (super coarse), and $20 - 70\ \mu\text{m}$ (super coarse/giant), respectively, for emitted particles. In comparison, the three dust modes, Aitken, accumulation, and coarse, in MAM4 cover size ranges of $0.010 - 0.10$, $0.10 - 1.0$, $1.0 - 10\ \mu\text{m}$, respectively.

When tuning the model to match the well-constrained global dust optical depth of approximately 0.030 in the visible band, we adjust the total emitted dust mass to match this total dust optical depth value. Because the mass extinction efficiency of fine dust peaks at visible wavelengths and a substantial portion of dust mass resides in the accumulation/fine and fine/coarse modes, visible-band dust optical depth provides a relatively strong constraint on dust particles within these size ranges. In contrast, this constraint weakens for coarser particles, whose contribution to visible-band dust optical depth is limited, while the observational global dust optical depth is available in the visible band. As a result, tuning based solely on visible-band dust optical depth offers limited leverage on super coarse and giant dust emissions. To overcome this limitation, alternative constraints, such as satellite-derived infrared-band dust optical depth, which is more sensitive to particles larger than $10\ \mu\text{m}$, or retrievals of dust effective diameter, are promising. However, their utility is currently limited by sparse observational coverage and the reliance on a single coarse mode in the retrieval process (Zheng et al., 2022).

In terms of deposition, contributions from differently sized dust modes vary substantially (Figure 8a). In MAM4, the single coarse mode used to simulate dust in the $1.0 - 10\ \mu\text{m}$ size range accounts for 99% of total dust deposition. In contrast, MAM10 reduces this contribution to 30% by simulating dust in this size range using the fine/coarse and medium-coarse modes. Super coarse/Giant dust dominates total deposition in MAM10, contributing 40% to the global deposition budget, while fine-mode dust contributes 1.0%, similar to that in MAM4.

The improved representation of dust through additional modes is also evident in the modeled $\text{PM}_{2.5}$ at the bottom model level. In MAM10, $\text{PM}_{2.5}$ is represented exclusively by fine dust modes (fine and fine/coarse), and the contributions of the three largest dust modes to $\text{PM}_{2.5}$ are

negligible, while the single coarse mode in MAM4 contributes about 45% of $PM_{2.5}$. Consequently, in MAM4 any attempt to increase coarse-mode aerosols also increased $PM_{2.5}$ aerosols, which limited the ability of the model to separately simulate fine and coarse mode aerosols.

Spatially, the distinct physical properties of different dust modes and the distribution of dust mass or number fluxes over them highlight their distinct roles in influencing the dust optical depth in the visible band, loadings, and deposition across regions (Figure 8b). Specifically, Figure 8b suggests the following three key findings.

First, the fine-coarse mode along with the accumulation mode dominates visible-band dust optical depth everywhere: in the tropics along the Intertropical Convergence Zone (ITCZ), and in high-latitude regions controlled by the accumulation mode, and the other regions dominated by the fine coarse mode. However, coarser dust modes (larger than $5.0\ \mu m$ in diameter) can contribute over 30% near or over source regions (Figure S5 in Supporting Information). Therefore, an inappropriate representation of dust aerosols larger than $5.0\ \mu m$ in diameter may lead to the misestimation of finer dust emission, given the tuning process used to achieve a global dust optical depth of 0.030 in the visible band. For example, neglecting the contribution of coarser modes to the global dust optical depth could result in excessive emissions of finer dust from source regions to compensate for the missing contribution from coarser particles.

Second, the fine/coarse mode dominates the dust loadings in most grid cells (Figure 8b) due to its longer atmospheric lifetime compared to coarser modes and its higher emission rates relative to dust in the accumulation mode.

Third, the two smallest dust modes (fine and fine/coarse) also dominate dust deposition in remote regions and along the ITCZ, whereas the giant dust mode's dominant influence remains confined to areas near dust sources due to its large size and short atmospheric lifetime. This spatial pattern (Figure 8b) underscores the critical role of the two smallest dust modes in transporting nutrients such as iron and phosphorus to ecosystems like the Amazon rainforest and the central Pacific, surpassing the contributions of other modes. The two smallest dust modes actually dominate most dust quantities, except for total global deposition, which is primarily simulated by the super coarse/giant dust mode.

7.4 Role of Dust Particles Larger Than 10 Microns in Diameter

Our model results suggest that dust particles larger than 10 μm in diameter are an important component of dust aerosols and should be included in models to estimate global and regional dust budgets, consistent with findings from previous studies using alternative models (Adebiyi et al., 2023). These particles contribute 70% of the total deposition flux and 30% of the total atmospheric loading in MAM10 (Figure 8a), which is slightly lower than a previous estimate of 35% (Adebiyi et al., 2023). While most of these particles (diameter larger than 10 μm) remain near dust source regions, such as the Sahara and the Sahel, a considerable amount of dust mass can be transported over long distances, as observed in various measurements (Prospero et al., 1970; Ryder et al., 2013; Ryder et al., 2018, 2019; Weinzierl et al., 2017; Weinzierl et al., 2009) and previously simulated (Adebiyi et al., 2023). Although these transported particles contribute far less to the total (size-integrated) dust budget than the global percentages shown in Table 4, they can still deposit onto remote ecosystems, including ocean basins, the Amazon Rainforest, Greenland, Antarctica, and the Tibetan Plateau, where they supply essential micro- and macronutrients.

Our calculations reveal a substantial increase in dust deposition across different regions when super coarse and giant dust particles are included, which is also revealed by a previous study (Adebiyi et al., 2023), along with the improved representation of particles in the 5.0 - 10 μm size range (Figure 9). Therefore, the inclusion of such super coarse and giant particles highlights the potential for a great upward revision of previously estimated dust budgets (Kok et al., 2023) and probably their climatic impacts, particularly through altering the land and ocean biogeochemistry, despite a disproportionally low impact of this fraction of dust on the direct radiative effect relative to their contribution to the dust budget, which will be quantified in our future papers.

Given the limited availability of high-quality observations, the new model likely underestimates dust deposition in the Southern Ocean, with values an order of magnitude lower than previous estimates (Kok et al., 2023), even without accounting for dust coarser than 20 μm (2.0 versus 25 Tg year^{-1}). The separation of sea salt from dust aerosols was intended to mitigate the excessive wet removal of dust observed in MAM4, particularly in regions downwind of South American

sources, such as the Patagonian Desert. The effect, however, is weaker than anticipated.

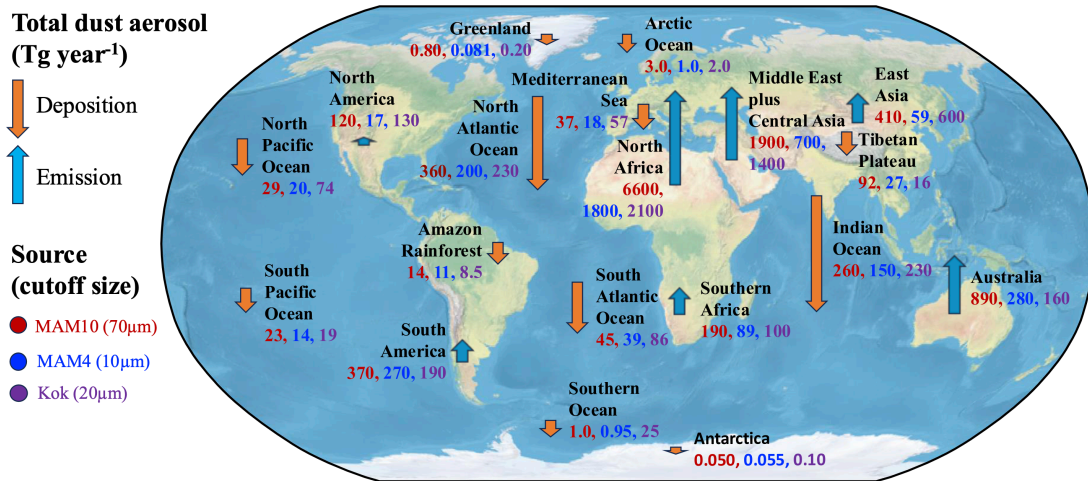


Figure 9. Regional dust emission and deposition budgets (Tg year⁻¹). Upward blue arrows represent dust emissions, while downward orange arrows indicate total (dry + wet) dust deposition. Numbers in red, blue, and purple correspond to results from MAM10 (dust geometric diameter smaller than 70 μm), MAM4 (dust geometric diameter smaller than 10 μm), and the best estimates (geometric diameter smaller than 20 μm) from Kok et al. (2023), which integrate observations with multi-model simulations. The marine geophysical definitions follow the shapefiles available at <https://marineregions.org/>, while the continental definitions follow Python's built-in geophysical files.

Although the global contribution of dust particles larger than 10 μm in diameter to the total dust optical depth in the visible band is small, their regional impact can be considerable. For example, campaign measurements over the Sahara Desert indicate a 40% contribution to the total dust optical depth at 0.55 μm (Ryder et al., 2018), which is similarly simulated here (Figure S5 in Supporting Information) and overall consistent with previous simulations (Adebisi et al., 2023). This suggests that, although excluding dust larger than 10 μm in diameter may not considerably affect the global visible-band dust optical depth, it could bias estimates of the finer dust emission toward higher values, especially near source regions such as in the Sahara Desert, to compensate for the missing contribution of dust larger than 10 μm in diameter, given that the model is tuned to a global visible-band dust optical depth of 0.030. Since fine-sized dust has a longer atmospheric lifetime and tends to scatter solar radiation more than it absorbs, this bias could

result in three key outcomes: (1) increased transport of dust away from source regions; (2) enhanced cooling effects everywhere; and (3) overestimation of $\text{PM}_{2.5}$ levels over source regions, such as Sahel and Sahara deserts.

8 Further Discussion and Conclusions

This study addresses two previously unresolved issues in CESM2: (1) the absence of dust particles larger than $10\text{ }\mu\text{m}$ in diameter, whose substantial presence is indicated by observations, and (2) the underrepresentation of dust mass and particle number between $1.0 - 10\text{ }\mu\text{m}$, which relies on a single mode that unrealistically dominates most dust quantities. These goals are achieved through the addition of modes representing larger particle diameters within the new mineral-resolved aerosol framework, MAM10. This new model also simulates more comprehensive dust emission physics, building upon previous work (Ke et al., 2022; Leung et al., 2024; Li et al., 2022; Liu et al., 2012), and uses a new EMIT atlas of surface soil mineralogy (Brodrick, Green, et al., 2023; Green et al., 2020) that is based upon a considerably larger number of measurements in dust source regions compared to pre-EMIT soil atlases (Claquin et al., 1999; Journet et al., 2014). A surface erodibility constraint is also imposed using the GUM dataset (Börker et al., 2018).

The model results compared to observations at varying distances from sources (Formenti & Di Biagio, 2024) indicate a reasonable representation of dust size distribution (Figure 5), including particles larger than 10 and up to $70\text{ }\mu\text{m}$ at emission. This improvement is mainly due to the introduction of new modes and a reduction in the modeled gravitational settling velocity of dust particles in the last three dust modes (corresponding to the largest diameters), consistent with previous studies (Drakaki et al., 2022; Ginoux, 2003; Meng et al., 2022), whereas the impact of the updated mass extinction efficiency associated with EMIT-derived iron oxides is negligible. With such improvement, the updated model maintains the overall dust cycle accuracy of MAM4 for particles under 10 or $2.5\text{ }\mu\text{m}$ when compared with observations for dust optical depth at visible wavelengths (Figure 1), surface elemental aluminum concentrations (a proxy for dust aerosols) (Figures 2 and 3), and total dust deposition (Figure 1).

The new MAM10 also more realistically simulates the seasonal variation of visible-band dust optical depth (Figure 4) and the distribution of dust across size ranges (Figure 8), addressing a key limitation in MAM4. In MAM4, a realistic $\text{PM}_{2.5}$ results in an unrealistic mass of dust at

larger diameters due to the influence of a single coarse mode representing both PM_{2.5} and coarser particles. By introducing additional modes at larger diameters, MAM10 allows the coarser dust fraction to vary independently of the fine fraction (accumulation mode), which now more appropriately dominates PM_{2.5}.

Although our results regarding dust larger than 10 μm in diameter are subject to large uncertainty (as discussed below), they emphasize the importance of simulating a fuller dust size distribution than what was typically done in previous studies (Ginoux et al., 2001; Li et al., 2022; Zender, Bian, et al., 2003) for accurately representing the dust cycle and its climatic effects. Dust particles coarser than 10 or 20 μm need to be included in both regional and global models for two reasons.

First, they substantially influence the simulated dust mass (Table 4 and Figure 9) (Adebisi et al., 2023) (Table 4). Including these particles will revise previous estimates of dust source and deposition budgets, and dust longwave direct radiative effect upward (Albani et al., 2014; Kok, et al., 2021; Kok et al., 2023; Li et al., 2022).

What is more important is that, even though do not proportionally affect the visible-band dust optical depth as to the dust deposition flux, dust particles coarser than 10 or 20 μm in diameter still can constitute a considerable fraction of the visible-band dust optical depth regionally (Figure S5 in Supporting Information). The common practice of tuning models to match a global visible-band dust optical depth target (e.g., 0.030) while omitting dust larger than 10 μm in diameter can introduce compensating biases, particularly in dust source regions. Specifically, models may overestimate the emissions of fine dust to reproduce the observed dust optical depth in the visible band, leading to an undue enhancement of long-range dust transport, surface cooling, and PM_{2.5} concentrations over regions like the Sahel and Sahara. These biases highlight the importance of explicitly representing dust larger than 10 μm in diameter, not only to refine dust source and sink estimates but also to improve assessments of dust-climate impacts through dust-radiation interactions (Kok et al., 2017) and effects on land and ocean biogeochemistry (Jickells et al., 2005; Mahowald, 2011; Mahowald et al., 2010, 2018; Mccutcheon et al., 2021; Meskhidze et al., 2005).

Regarding the dust mineral composition, while a systematic, clean comparison of simulated mineralogy using EMIT and pre-EMIT soil mineral atlases is reserved for a forthcoming study,

1229 this study highlights the effects of key model developments on simulated mineral fractions and
1230 their consistency with observations. Specifically, the new MAM10 extends the capabilities of
1231 MAM4 by enabling the simulation of minerals in dust aerosol particles larger than 10 or 20 μm
1232 in diameter, although challenges remain in reproducing observed mineral mass fractions across
1233 different size categories (Figures 7 and S4 in Supporting Information). This improvement,
1234 compared to previous studies, provides insights into the climatic impacts of dust, which remain
1235 highly uncertain, especially when considering surface soil mineralogy (Li et al., 2021) and dust
1236 size distribution (Kok et al., 2017; Mahowald et al., 2014). The revised assessment of these
1237 impacts, along with more detailed mineral evaluations, will be discussed in our forthcoming
1238 paper(s).

1239 The remaining discrepancies between modeled and observed dust mineral aerosols may stem
1240 from the known deficiencies in the EMIT soil mineral atlas (e.g., misidentification of certain
1241 nano-hematite-nano-goethite mixtures as jarosite) and from the representations of iron oxides in
1242 the model (e.g., omission of nano-iron oxides). Furthermore, the EMIT instrument cannot
1243 directly detect quartz and feldspar, as these minerals lack diagnostic VSWIR (Visible to
1244 Shortwave Infrared) absorption features. Instead, their presence is inferred in part from existing
1245 soil mineralogy atlases, which carry substantial uncertainties in representing their abundances in
1246 clay- and silt-sized categories. All these limitations, whose significance may depend on particle
1247 size, also hinder models from accurately capturing the size dependence of key mineral
1248 components (e.g., iron oxides and K-feldspar), and, consequently, from reliably quantifying
1249 dust's climatic impacts. Additional sources of error include inaccuracies in dust size distribution,
1250 emission, transport, and deposition processes; observational uncertainties (including the limited
1251 availability of mineralogical composition measurements for dust aerosols); and the model-
1252 observation comparison methodology. Therefore, these discrepancies do not necessarily provide
1253 a complete reflection of the accuracy of the soil mineralogical characterization in the EMIT atlas.

1254 Despite the advancements, several challenges remain that hinder the model's ability to accurately
1255 simulate dust cycles with a physical basis, particularly in reproducing dust size distributions.

1256 First, there is a lack of precise measurements of the size distribution of mineral dust in the size
1257 range larger than 20 μm in diameter, especially in source regions (Formenti & Di Biagio, 2024),
1258 limiting the ability to constrain emission and atmospheric abundance of dust (mineral) aerosols

in this size range (primarily applied to quartz, feldspar and possibly carbonates. Iron oxides and phyllosilicates are typically small, less than a couple microns). This scarcity stems from various factors, including a historical underestimation of the importance of larger dust particles, instrumental challenges (e.g., low sampling efficiencies of instrument inlets) for airborne measurements (Adebiyi et al., 2023), and the rarity of field campaigns equipped to capture a full dust size distribution, given that instruments, such as light optical aerosol counters (Ryder et al., 2013, 2019; Ryder et al., 2018; Weinzierl et al., 2017; Weinzierl et al., 2009) or multiple aerosol spectrometers, only detect subsets of the dust size distribution. Consequently, our global estimates of total dust and the contributions of particles larger than 10 or 20 μm in diameter are highly uncertain, which are sensitive to the size distribution representation in the model.

A second challenge involves simulating dust particles larger than 5.0 μm in diameter, which may behave differently from finer particles in terms of transport, deposition, and radiative effects. An accurate representation of their transport and deposition could be crucial for quantifying their regional and global impacts. While reducing the gravitational settling velocity of large dust particles, particularly at geometric diameters larger than 20 μm , can achieve certain improvements like those shown here (Figure 5) and in previous studies (Drakaki et al., 2022; Ginoux, 2003; Meng et al., 2022), the physical mechanisms for slowing descent of these particles remain unclear (van der Does et al., 2018), as earlier studies also noticed (Betzer et al., 1988; Mahowald et al., 2005).

Recent findings suggest potential mechanisms for maintaining particles aloft, such as topography (Heisel et al., 2021; Rosenberg et al., 2014), electric forces on charged particles (van der Does et al., 2018; Toth et al., 2020), underrepresented uplifts by convection events (combining the other possible mechanisms or multiple uplifts occurring within a long-lived system) (van der Does et al., 2018) or turbulence (radiation- or shear-induced) in the free troposphere (Rodakoviski et al., 2023), horizontal and vertical spatial resolutions of models (Feng et al., 2022) or aerosol splitting processes in models (Wan et al., 2024), and variations in particle shape and orientation (Bagheri & Bonadonna, 2016; Huang et al., 2020; Mallios et al., 2020). Testing these mechanisms is beyond the scope of this study but deserves future investigations. Here, we only approximate the effects by adjusting the gravitational settling velocity for dust particles represented by the last three dust modes corresponding to the largest diameters. However, this adjustment is applied uniformly across regions, ignoring potential spatial variability. Probably in part because of the

uniform adjustment, the model remains unable to reproduce the slow removal rate of giant dust particles during source-to-medium-range transport (Figure 5).

The third challenge is on the accurate representation of the physical (e.g., optical) properties of dust particles larger than 20 μm in diameter based on their mineral composition, which affects dust climatic impacts. Translating soil composition into aerosol mineralogy is particularly challenging for iron oxides and quartz in giant dust aerosol particles due to the scarcity of measurements and the need for advanced techniques. Dust aerosol particles larger than 20 μm in diameter are difficult to sample and analyze compared to particles smaller than 10 μm in diameter. Uncertainties stemming from the representation of atmospheric processes, such as chemical reactions and cloud processing (Langmann, 2013; Longo et al., 2016; Usher et al., 2003), are likely limited, given the low number concentration and short lifetime of dust particles larger than 20 μm .

Fourth, several factors influencing the modeled dust size distribution, such as the prescribed geometric standard deviation as a global constant and settling velocity for particles larger than 5.0 μm in diameter, remain poorly constrained. Empirical tuning is used in this study to match observed size distributions. While observationally derived geometric standard deviations can be prescribed, missing or inaccurate physics, such as mechanisms for maintaining particles aloft, or other unknown errors may have hindered achieving the intended outcomes. Therefore, we adjusted dust parameters to match the observed size distribution. However, there is still room for further refinement of either dust mode parameters or the gravitational settling velocity (Figure 5), which might lead to considerably different results.

Additional approaches to further constrain super coarse and giant dust particles are to match observed dust optical depth at longwave wavelengths or effective diameter measurements (Zheng et al., 2022). However, uncertainties in the dust optical depth retrievals at longwave wavelengths could make this challenging. Sparse observations of effective diameters—limited by assumptions such as mono-modal particle size distributions, the near absence of reliable observations over land (Zheng et al., 2022), and uncertainties in the emitting temperature of dust layers, partly due to substantial variability in the vertical structure of dust plumes from one event to another (Li & Sokolik, 2018)—further complicate this method. From these perspectives, future constraints on effective diameter retrievals could potentially reduce uncertainties in

modeling the large (especially diameters larger than 20 μm) dust particle cycle as well, in addition to those in longwave dust radiative effect estimates. These approaches are deferred to future investigations.

Fifth, reproducing the dust cycle across different environments and measurements remains challenging. The complex interactions of factors like surface winds, vegetation, and soil moisture dynamics (Kok et al., 2012; Shao, 2008) govern dust emission, transport, and deposition. Uncertainties in model parameterization that affect these processes further complicate predictions for different dust phases. As a result, like MAM4 (Li et al., 2022), the new model cannot match the observed dust deposition, visible-band dust optical depth, and surface aluminum elemental PM_{10} concentrations simultaneously (Figures 1 and 3), which has been recognized for more than a decade (Huneeus et al., 2011).

Sixth, MAM10 does not include the effect of preexisting ice crystals in cirrus considered in CAM5 (Shi et al., 2015) for dust of all size ranges, which is deferred for future studies. Excluding this mechanism could lead to an overestimation of simulated ice nuclei concentrations as preexisting ice crystals may inhibit homogeneous freezing. In addition, dust-cloud interactions (DeMott et al., 2003; Karydis et al., 2011) are not included in this model for particles with diameters larger than 20 μm . However, their impact is likely minimal, as cloud effects scale with aerosol number concentrations (Andreae & Rosenfeld, 2008), which are very low for dust larger than 20 μm in diameter.

Lastly, MAM10 does not account for additional constituents except sulfate that may be internally mixed with dust aerosols, such as soot and primary biological particles (e.g., microorganisms and biological material fragments) (Kellogg & Griffin, 2006; Shinn et al., 2000), which exhibit regional contrasts. The mixing of these species with dust aerosols is excluded from the MAM10 framework presented here. Below, we outline the specific reasons, using sea salt as an example; however, future studies may need to investigate the impact of an alternative treatment, in which dust is internally mixed with these species, on simulations of the dust cycle and its climatic effects.

The external mixing of dust with the other species except sulfate is inherited from previous aerosol model versions, MAM7 and MAM9, for simplicity. Here, we advance the model to

simulate a fuller and more accurate size distribution of dust aerosols. While MAM4 simulates dust as a mixture with other components, such as sea salt, the mechanisms driving the mixing of dust particles and sea salt remain insufficiently detailed (Andreae et al., 1986; Zhang et al., 2005). The mixing state of dust and sea salt also depends on the region. Observations show infrequent internal mixing of African dust with sea salt, particularly during peak dust outbreak seasons when the largest transport occurs across the Atlantic Ocean (Kandler et al., 2007; Reid et al., 2003) and the dust plume is elevated. In these scenarios, African dust particles are typically transported above the marine boundary layer (Karyampudi et al., 1999) and dust layers remain distinct from it (Reid et al., 2002), resulting in frequently low sea salt mass fractions (less than 10%) in dust plumes (Chiapello et al., 1999). In contrast, East Asian dust transported eastward shows higher degrees of internal mixing with soluble salts (Niimura et al., 1998), including sea salt, ranging from 18 to 42% by volume (Osada, 2013). Over 60% of dust particles collected at Japanese islands, after several hours of transport through marine air, were found internally mixed with sea salt (Okada et al., 1990; Niimura et al., 1998; Zhang et al., 2003b). Based upon these findings, the separation of dust and sea salt in MAM10 may be not a good assumption for East Asian dust aerosols, potentially biasing estimates of their wet removal rates and climatic effects. Moreover, observations on the mixing state of dust with sea salt, especially in the Southern Ocean, are far more limited. For the mixing of primary biological particles with dust aerosols, some attempts exist (Adachi et al., 2020; Brodsky et al., 2023), but the results remain preliminary.

Beyond addressing current limitations, the new model developed in this study allows a more accurate and complete representation of the dust climatic impacts than previous CAM versions. It complements existing models (Di Biagio et al., 2020, Ke et al., 2022, Wang et al., 2024) in quantifying the role of super coarse and giant dust particles in dust-radiation interactions and their influence on modeling trace metal deposition, which is critical for terrestrial and ocean biogeochemistry (Brodsky et al., 2023; Lu et al., 2024; Mahowald et al., 2018; Wong et al., 2021).

The modeling framework developed here not only improves the representation of large dust particles but could also be used to simulate other aerosols with broad size distributions, such as volcanic ash, whose size often exceeds 10 μm in diameter (Brown et al., 2012).

Recognizing all the unresolved issues, it is imperative for future research endeavors to encompass a more comprehensive analysis, incorporating a broader range of species present in dust aerosols and a more advanced, physically based modeling approach to simulate large-size dust aerosols with observational constraints. This refinement of the modeling approaches in the future will help improve accuracy in regional and global climate assessments, enhancing our understanding of aerosol composition and their roles in the Earth-Human-Climate system.

Acknowledgments

L.L., N.M.M., R.L.M., and R.N.C. received support from the NASA EMIT project. EMIT is supported by the NASA Earth Venture Instrument program under the Earth Science Division of the Science Mission Directorate. L.L. and N.M.M. also acknowledge assistance from the Department of Energy (DOE) under grant DE-SC0021302, the high-performance computing resources from Derecho provided by National Center for Atmospheric Research (NCAR)'s Computational and Information Systems Laboratory (CISL), sponsored by the National Science Foundation (NSF), and a NASA Interdisciplinary Science (IDS) project under grant 80NSSC20K1674. C.P.G.P., M.G.A., and V.O. acknowledge funding by the European Research Council under the Horizon 2020 research and innovation program through the ERC Consolidator Grant FRAGMENT under grant 773051, the AXA Research Fund through the AXA Chair on Sand and Dust Storms at BSC, and the European Union's Horizon 2020 research and innovation program under grant agreement No 821205 (FORCeS). C.P.G.P. and V.O. also acknowledge Grant PID2022-140365OB-I and M.G.A. acknowledges Grant PID2022-139362OB-I00, both funded by MICIU/AEI/10.13039/501100011033 and by ERDF, EU. R.L.M. also received support from the NASA Modeling, Analysis, and Prediction Program under grant NNG14HH42I. J.F.K. acknowledges support from the NSF Directorate for Geosciences under grants 1856389 and 2151093. P.F. and C.D.B. received support from the DustClim project, which is part of ERA4CS, an ERA-NET project initiated by JPI Climate and funded by FORMAS (SE), DLR (DE), BMWFW (AT), IFD (DK), MINECO (ES), and ANR (FR) with co-funding from the European Union's Horizon program under grant 690462. P.F. and C.D.B. also received support from the French national program LEFE/INSU (Les Enveloppes Fluides et l'Environnement/Institut National des Sciences de l'Univers) and by the OSU-EFLUVE (Observatoire des Sciences de l'Univers-Enveloppes Fluides de la Ville à l'Exobiologie) through

dedicated research funding to the RED-DUST project, and the European Union's Horizon 2020 research and innovation program through the EUROCHAMP-2020 Infrastructure Activity under grant 730997. C.D.B. was supported by the Centre National des Etudes Spatiales (CNES) and by the CNRS via the Labex L-IPSL, which is funded by the ANR under grant ANR-10-LABX-0018. D.M.L. acknowledges support from the NSF NCAR Advanced Study Program (ASP) Postdoctoral Fellowship and from the Quadrature Climate Foundation (QCF) under grant 01-21-000349. A portion of this research was performed at the Jet Propulsion Laboratory (JPL), California Institute of Technology, under a contract with NASA. We thank Raymond F. Kokaly, Gregg A. Swayze, Francisco Ochoa, Abigail Keebler, and Bethany L. Ehlmann for their contributions to the generation of the EMIT soil mineral atlas, and John Dunne for conducting the GFDL internal review.

Author Contributions

L.L. conceived the study, developed the MAM10 code in CAM6, performed the model simulations, conducted the formal analysis, generated the figures, and wrote the initial manuscript draft. N.M.M. provided the elemental data and supervised the work. X.L. and Z.K. supplied the MAM9 code in CAM5. M.G.A. conducted the mineral evaluation. D.M.L. and J.F.K. supplied the new dust emission scheme code. M.G.A., C.P.G.P., R.L.M., V.O., P.G., P.G.B., D.R.T., R.N.C., G.S.O., R.O.G., and B.Z. contributed to the development of the EMIT soil mineral atlas. S.A. provided the post-processed AERONET data, and A.A.A. derived the geometric standard deviations for the five dust modes in MAM10, which L.L. subsequently retuned to improve model performance. All authors reviewed and provided comments on the original manuscript draft.

Code and Data Availability Statement

The core component of the CAM6-MAM4 and observations (AERONET dust aerosol optical depth, surface concentrations, and deposition fluxes) are available in a publicly accessible repository at <https://doi.org/10.5281/zenodo.6989502> and are documented in detail by Li et al. (2022). The MAM10 code will be available in a publicly accessible repository. The EMIT soil mineralogy data is publicly available through the NASA LP DAAC, subject to their data use policy. The elemental aluminum data is detailed by Mahowald et al. (2024) and archived with the link of <https://zenodo.org/records/11391232>. Detailed documentation of the observed mineral

fractions can be found in previous studies (Gonçalves Ageitos et al., 2023; Perlwitz et al., 2015b, 2015a) and obtained by contacting the respective corresponding authors. The database of dust size distribution provided in Formenti and Di Biagio (2024) is available in the EaSy data repository (<https://www.easydata.earth/#/public/home>).

References

- Adachi, K., Oshima, N., Gong, Z., De Sá, S., Bateman, A. P., Martin, S. T., et al. (2020). Mixing states of Amazon basin aerosol particles transported over long distances using transmission electron microscopy. *Atmospheric Chemistry and Physics*, 20(20), 11923–11939. <https://doi.org/10.5194/acp-20-11923-2020>
- Adebiyi, A., Kok, J., Wang, Y., Ito, A., Ridley, D., Nabat, P., & Zhao, C. (2020). Dust Constraints from joint Observational-Modelling-experimental analysis (DustCOMM): Comparison with measurements and model simulations. *Atmospheric Chemistry and Physics*, 829–863. <https://doi.org/10.5194/acp-2019-484>
- Adebiyi, A., Kok, J. F., Murray, B. J., Ryder, C. L., Stuut, J.-B. W., Kahn, R. A., et al. (2023). A review of coarse mineral dust in the Earth system. *Aeolian Research*, 60, 100849. <https://doi.org/10.1016/j.aeolia.2022.100849>
- Adebiyi, A. A., & Kok, J. F. (2020). Climate models miss most of the coarse dust in the atmosphere. *Science Advances*, 6(15), 1–10. <https://doi.org/10.1126/sciadv.aaz9507>
- Albani, S., Mahowald, N. M., Perry, A. T., Scanza, R. A., Zender, C. S., Heavens, N. G., et al. (2014). Improved dust representation in the Community Atmosphere Model. *Journal of Advances in Modeling Earth Systems*, 6(3), 541–570. <https://doi.org/10.1002/2013MS000279>
- Andreae, M. O., & Rosenfeld, D. (2008). Aerosol-cloud-precipitation interactions. Part 1. The nature and sources of cloud-active aerosols. *Earth-Science Reviews*, 89(1–2), 13–41. <https://doi.org/10.1016/j.earscirev.2008.03.001>
- Bagheri, G., & Bonadonna, C. (2016). On the drag of freely falling non-spherical particles. *Powder Technology*, 301, 526–544. <https://doi.org/10.1016/j.powtec.2016.06.015>
- Bagnold, R. A. (1941). *The physics of blown sand and desert dunes*. Mineola, New York: Dover Publication Inc. <https://doi.org/10.1007/978-94-009-5682-7>
- Baker, A. R., & Jickells, T. D. (2006). Mineral particle size as a control on aerosol iron solubility. *Geophysical Research Letters*, 33(17), 1–4. <https://doi.org/10.1029/2006GL026557>
- Betzer, P. R., Carder, K. L., Duce, R. A., Merrill, J. T., Tindale, N. W., Uematsu, M., et al. (1988). Long-range transport of giant mineral aerosol particles. *Nature*, 336, 568–571. <https://doi.org/10.1038/336568a0>
- Bhattachan, A., Okin, G. S., Zhang, J., Vimal, S., & Lettenmaier, D. P. (2019). Characterizing the Role of Wind and Dust in Traffic Accidents in California. *GeoHealth*, 3(10), 328–336. <https://doi.org/10.1029/2019GH000212>

- 1471 Börker, J., Hartmann, J., Amann, T., & Romero-Mujalli, G. (2018). Terrestrial sediments of the earth: Development
1472 of a global unconsolidated sediments map database (gum). *Geochemistry, Geophysics, Geosystems*, 19(4),
1473 997–1024. <https://doi.org/10.1002/2017GC007273>
- 1474 Brodrick, P. G., Clark, R. N., Swayze, G. A., Ehlman, B., Keebler, A., Thompson, D. R., & Green, R. O. (2023).
1475 *Earth Surface Mineral dust source InvesTigation (EMIT) EMIT L2b Algorithm: Mineral Detection and*
1476 *Related Products at the Pixel Scale Theoretical Basis*. Pasadena, California 91109-8099.
- 1477 Brodrick, P. G., Okin, G., Ochoa, F., Thompson, D., Clark, R., Ehlmann, B., et al. (2023). EMIT L3 Aggregated
1478 Mineral Spectral Abundance and Uncertainty 0.5 Deg V001 [Data set].
1479 <https://doi.org/https://doi.org/10.5067/EMIT/EMITL3ASA.001>
- 1480 Brodrick, P. G., Green, R. O., Thompson, D. R., Mahowald, N. M., Clark, R. N., Swayze, G. A., et al. (2023). The
1481 Earth Surface Mineral Dust Source Investigation (EMIT): Global Distributions of Mineralogy in Arid Lands
1482 (pp. 11–15). San Francisco, CA: American Geophysical Union Fall Meeting. <https://doi.org/GC53B-05>
- 1483 Brodsky, H., Calderón, R., Hamilton, D. S., Li, L., Miles, A., Pavlick, R., et al. (2023). Assessing long-distance
1484 atmospheric transport of soilborne plant pathogens. *Environmental Research Letters*, 18(10).
1485 <https://doi.org/10.1088/1748-9326/acf50c>
- 1486 Brown, R. J., Bonadonna, C., & Durant, A. J. (2012). A review of volcanic ash aggregation. *Physics and Chemistry*
1487 *of the Earth*, 45–46, 65–78. <https://doi.org/10.1016/j.pce.2011.11.001>
- 1488 Bullard, J. E. (2017). The distribution and biogeochemical importance of highlatitude dust in the Arctic and
1489 Southern Ocean- Antarctic regions. *Journal of Geophysical Research*, 122(5), 3098–3103.
1490 <https://doi.org/10.1002/2016JD026363>
- 1491 Chen, H., Laskin, A., Baltrusaitis, J., Gorski, C. A., Scherer, M. M., & Grassian, V. H. (2012). Coal Fly Ash as a
1492 Source of Iron in Atmospheric Dust. *Environmental Science & Technology*, 46(4), 2112–2120.
1493 <https://doi.org/10.1021/es204102f>
- 1494 Chiapello, I., Bergametti, B. M., Gilles, Chatenet, B., Dulac, F., Jankowiak, I., et al. (1999). Contribution of the
1495 different aerosol species to the aerosol mass load and optical depth over the northeastern tropical Atlantic.
1496 *Journal of Geophysical Research*, 104(D4), 4025–4035. <https://doi.org/10.1029/1998JD200044>
- 1497 Claquin, T., Schulz, M., & Balkanski, Y. (1999). Modeling the mineralogy of atmospheric dust sources. *Journal of*
1498 *Geophysical Research*, 104(D18), 22,222–243,256. [https://doi.org/10.1016/S1352-2310\(03\)00506-5](https://doi.org/10.1016/S1352-2310(03)00506-5)
- 1499 Clark, R. N., & Roush, T. L. (1984). Reflectance spectroscopy: quantitative analysis techniques for remote sensing
1500 applications. *Journal of Geophysical Research*, 89(B7), 6329–6340.
1501 <https://doi.org/10.1029/JB089iB07p06329>
- 1502 Clark, Roger N. (2024). PSI-edu/spectroscopy-tetracorder: Tetracorder 5.27 with expert systems to 5.27e + specpr,
1503 spectral libraries, and radiative transfer models (v5.27.0). *Zenodo*.
1504 <https://doi.org/https://doi.org/10.5281/zenodo.11204505>

- Clark, Roger N., Swayze, G. A., Eric Livo, K., Brodrick, P. G., Dobrea, E. N., Vijayarangan, S., et al. (2024). Imaging Spectroscopy: Earth and Planetary Remote Sensing with the PSI Tetracorder and Expert Systems from Rovers to EMIT and Beyond. *Planetary Science Journal*, 5(12). <https://doi.org/10.3847/PSJ/ad6c3a>
- Comola, F., Kok, J. F., Chamecki, M., & Martin, R. L. (2019). The Intermittency of Wind-Driven Sand Transport. *Geophysical Research Letters*, 46(22), 13430–13440. <https://doi.org/10.1029/2019GL085739>
- Darmenova, K., Sokolik, I. N., Shao, Y., Marticorena, B., & Bergametti, G. (2009). Development of a physically based dust emission module within the weather research and forecasting (WRF) model: Assessment of dust emission parameterizations and input parameters for source regions in central and east asia. *Journal of Geophysical Research Atmospheres*, 114(14). <https://doi.org/10.1029/2008JD011236>
- DeMott, P. J., Sassen, K., Poellot, M. R., Baumgardner, D., Rogers, D. C., Brooks, S. D., et al. (2003). African dust aerosols as atmospheric ice nuclei. *Geophysical Research Letters*, 30(14), 1732, doi:10/1029/2003GL017410, 2003.
- Van Der Does, M., Korte, L. F., Munday, C. I., Brummer, G. J. A., & Stuut, J. B. W. (2016). Particle size traces modern Saharan dust transport and deposition across the equatorial North Atlantic. *Atmospheric Chemistry and Physics*, 16(21), 13697–13710. <https://doi.org/10.5194/acp-16-13697-2016>
- van der Does, M., Knippertz, P., Zschenderlein, P., Giles Harrison, R., & Stuut, J. B. W. (2018). The mysterious long-range transport of giant mineral dust particles. *Science Advances*, 4(12), 1–9. <https://doi.org/10.1126/sciadv.aau2768>
- Drakaki, E., Amiridis, V., Tsekeri, A., Gkikas, A., Proestakis, E., & Drakaki, C. E. (2022). Modeling coarse and giant desert dust particles. *Atmospheric Chemistry and Physics*, 22, 12727–12748. <https://doi.org/10.5194/acp-22-12727-2022>
- Dubovik, O., Smirnov, A., Holben, B. N., King, M. D., Kaufman, Y. J., Eck, T. F., & Slutsker, I. (2000). Accuracy assessments of aerosol optical properties retrieved from Aerosol Robotic Network (AERONET) Sun and sky radiance measurements. *Journal of Geophysical Research*, 105(D8), 9791–9806. <https://doi.org/10.1029/2000JD900040>
- Dupont, S., Bergametti, G., Marticorena, B., & Simoëns, S. (2013). Modeling saltation intermittency. *Journal of Geophysical Research Atmospheres*, 118(13), 7109–7128. <https://doi.org/10.1002/jgrd.50528>
- Easter, R. C., Ghan, S. J., Zhang, Y., Saylor, R. D., Chapman, E. G., Laulainen, N. S., et al. (2004). MIRAGE: Model description and evaluation of aerosols and trace gases. *Journal of Geophysical Research D: Atmospheres*, 109(20), 1–46. <https://doi.org/10.1029/2004JD004571>
- Eyring, V., Bony, S., Meehl, G. A., Senior, C. A., Stevens, B., Stouffer, R. J., & Taylor, K. E. (2016). Overview of the Coupled Model Intercomparison Project Phase 6 (CMIP6) experimental design and organization. *Geoscientific Model Development*, 9(5), 1937–1958. <https://doi.org/10.5194/gmd-9-1937-2016>

- Falkovich, A. H., Ganor, E., Levin, Z., Formenti, P., & Rudich, Y. (2001). Chemical and mineralogical analysis of individual mineral dust particles. *Journal of Geophysical Research*, 106(D16), 18029–18036. <https://doi.org/10.1029/2000JD900430>
- Fécan, F., Marticorena, B., & Bergametti, G. (1998). Parametrization of the increase of the aeolian erosion threshold wind friction velocity due to soil moisture for arid and semi-arid areas. *Annales Geophysicae*, 17(1), 149–157. <https://doi.org/10.1007/s00585-999-0149-7>
- Feng, Y., Wang, H., Rasch, P. J., Zhang, K., Lin, W., Tang, Q., et al. (2022). Global Dust Cycle and Direct Radiative Effect in E3SM Version 1: Impact of Increasing Model Resolution. *Journal of Advances in Modeling Earth Systems*, 14(7). <https://doi.org/10.1029/2021MS002909>
- Formenti, P., & Di Biagio, C. (2024). Large synthesis of in situ field measurements of the size distribution of mineral dust aerosols across their life cycles. *Earth System Science Data*, 16(11), 4995–5007. <https://doi.org/10.5194/essd-16-4995-2024>
- Formenti, P., Andreae, M. O., Lange, L., Roberts, G., Cafmeyer, J., Rajta, I., et al. (2001). Saharan dust in Brazil and Suriname during the Large-Scale Biosphere-Atmosphere Experiment in Amazonia (LBA)-Cooperative LBA Regional Experiment (CLAIRE) in March 1998. *J. Geophys. Res.*, 106(D14), 14919–14934.
- Gelaro, R., McCarty, W., Suárez, M. J., Todling, R., Molod, A., Takacs, L., et al. (2017). The modern-era retrospective analysis for research and applications, version 2 (MERRA-2). *Journal of Climate*, 30(14), 5419–5454. <https://doi.org/10.1175/JCLI-D-16-0758.1>
- Ghan, S. J., & Zaveri, R. A. (2007). Parameterization of optical properties for hydrated internally mixed aerosol. *Journal of Geophysical Research Atmospheres*, 112(10), 1–10. <https://doi.org/10.1029/2006JD007927>
- Ginoux, P. (2003). Effects of nonsphericity on mineral dust modeling. *J. Geophys. Res.*, 108(D2), 4052, doi: 1029/2002/JD002516.
- Ginoux, P., Chin, M., Tegen, I., Prospero, J. M., Holben, B. N., Dubovik, O., & Lin, S.-J. (2001). Sources and distribution of dust aerosols with the GOCART model. *Journal of Geophysical Research*, 106(D17), 20255–20273. <https://doi.org/https://doi.org/10.1029/2000JD000053>
- Gliß, J., Mortier, A., Schulz, M., Andrews, E., Balkanski, Y., Bauer, S. E., et al. (2021). AeroCom phase III multi-model evaluation of the aerosol life cycle and optical properties using ground- And space-based remote sensing as well as surface in situ observations. *Atmospheric Chemistry and Physics*, 21(1), 87–128. <https://doi.org/10.5194/acp-21-87-2021>
- Gonçalves Ageitos, M., Obiso, V., Miller, R. L., Jorba, O., Klose, M., Dawson, M., et al. (2023). Modeling dust mineralogical composition: sensitivity to soil mineralogy atlases and their expected climate impacts. *Atmospheric Chemistry and Physics*, 23(15), 8623–8657. <https://doi.org/10.5194/acp-23-8623-2023>
- Goudie, A. S. (2014). Desert dust and human health disorders. *Environment International*. Elsevier Ltd. <https://doi.org/10.1016/j.envint.2013.10.011>

- Green, R. O., Mahowald, N., Ung, C., Thompson, D. R., Bator, L., Bennet, M., et al. (2020). The Earth Surface Mineral Dust Source Investigation: An Earth Science Imaging Spectroscopy Mission. *IEEE Aerospace Conference Proceedings*. <https://doi.org/10.1109/AERO47225.2020.9172731>
- Groot Zwaafink, C. D., Grythe, H., Skov, H., & Stohl, A. (2016). Substantial contribution of northern high-latitude sources to mineral dust in the Arctic. *Journal of Geophysical Research*, 121(22), 13,678–13,697. <https://doi.org/10.1002/2016JD025482>
- Hapke, B. (1981). Bidirectional reflectance spectroscopy: 1. Theory. *Journal of Geophysical Research: Solid Earth*, 86(B4), 3039–3054. <https://doi.org/10.1029/jb086ib04p03039>
- Heisel, M., Chen, B., Kok, J. F., & Chamecki, M. (2021). Gentle Topography Increases Vertical Transport of Coarse Dust by Orders of Magnitude. *Journal of Geophysical Research: Atmospheres*, 126(14), 1–16. <https://doi.org/10.1029/2021jd034564>
- Huang, Y., Kok, J. F., Kandler, K., Lindqvist, H., Nousiainen, T., Sakai, T., et al. (2020). Climate Models and Remote Sensing Retrievals Neglect Substantial Desert Dust Asphericity. *Geophysical Research Letters*, 47(6), 1–11. <https://doi.org/10.1029/2019GL086592>
- Huang, Y., Kok, J. F., Saito, M., & Muñoz, O. (2023). Single-scattering properties of ellipsoidal dust aerosols constrained by measured dust shape distributions. *Atmospheric Chemistry and Physics*, 2557–2577. <https://doi.org/https://doi.org/10.5194/acp-23-2557-2023>
- Huneeus, N., Schulz, M., Balkanski, Y., Griesfeller, J., Prospero, J., Kinne, S., et al. (2011). Global dust model intercomparison in AeroCom phase i. *Atmospheric Chemistry and Physics*, 11(15), 7781–7816. <https://doi.org/10.5194/acp-11-7781-2011>
- Jickells, T. D., An, Z. S., Andersen, K. K., Baker, A. R., Bergametti, C., Brooks, N., et al. (2005). Global iron connections between desert dust, ocean biogeochemistry, and climate. *Science*, 308(5718). <https://doi.org/10.1126/science.1105959>
- Jones, A. C., Hill, A., Hemmings, J., Lemaitre, P., Quérel, A., Ryder, C. L., & Woodward, S. (2022). Below-cloud scavenging of aerosol by rain: a review of numerical modelling approaches and sensitivity simulations with mineral dust in the Met Office’s Unified Model. *Atmospheric Chemistry and Physics*, 22(17), 11381–11407. <https://doi.org/10.5194/acp-22-11381-2022>
- Journet, E., Balkanski, Y., & Harrison, S. (2014). A new data set of soil mineralogy for dust-cycle modeling. *Atmospheric Chemistry and Physics*, 14, 2014–3801.
- Kalashnikova, O. V., & Sokolik, I. N. (2004). Modeling the radiative properties of nonspherical soil-derived mineral aerosols. *Journal of Quantitative Spectroscopy and Radiative Transfer*, 87(2), 137–166. <https://doi.org/10.1016/j.jqsrt.2003.12.026>
- Kandler, K., Benker, N., Bundke, U., Cuevas, E., Ebert, M., Knippertz, P., et al. (2007). Chemical composition and complex refractive index of Saharan Mineral Dust at Izaña, Tenerife (Spain) derived by electron microscopy. *Atmospheric Environment*, 41(37), 8058–8074. <https://doi.org/10.1016/j.atmosenv.2007.06.047>

- Kandler, K., Schütz, L., Deutscher, C., Ebert, M., Hofmann, H., Jäckel, S., et al. (2009). Size distribution, mass concentration, chemical and mineralogical composition and derived optical parameters of the boundary layer aerosol at Tinfou, Morocco, during SAMUM 2006. *Tellus, Series B: Chemical and Physical Meteorology*, 61(1), 32–50. <https://doi.org/10.1111/j.1600-0889.2008.00385.x>
- Karyampudi, V. M., Palm, S. P., Reagen, J. A., Fang, H., Grant, W. B., Hoff, R. M., et al. (1999). Validation of the Saharan Dust Plume Conceptual Model Using Lidar, Meteosat, and ECMWF Data. *Bulletin American Meteorological Society*, 80(6), 1045–1075. [https://doi.org/10.1175/1520-0477\(1999\)080<1045:VOTSDP>2.0.CO;2](https://doi.org/10.1175/1520-0477(1999)080<1045:VOTSDP>2.0.CO;2)
- Karydis, V. A., Kumar, P., Barahona, D., Sokolik, I. N., & Nenes, A. (2011). On the effect of dust particles on global cloud condensation nuclei and cloud droplet number. *Journal of Geophysical Research Atmospheres*, 116(23). <https://doi.org/10.1029/2011JD016283>
- Ke, Z., Liu, X., Wu, M., Shan, Y., & Shi, Y. (2022). Improved Dust Representation and Impacts on Dust Transport and Radiative Effect in CAM5. <https://doi.org/10.1029/2021MS002845>
- Kellogg, C. A., & Griffin, D. W. (2006). Aerobiology and the global transport of desert dust. *Trends in Ecology and Evolution*, 21(11), 638–644. <https://doi.org/10.1016/j.tree.2006.07.004>
- Klose, M., Jorba, O., Ageitos, M. G., Escribano, J., Dawson, M. L., Obiso, V., et al. (2021). Mineral dust cycle in the Multiscale Online Nonhydrostatic Atmosphere Chemistry model (MONARCH) Version 2 . 0. *Geoscientific Model Development*, 14(10), 6403–6444. <https://doi.org/10.5194/gmd-14-6403-2021>
- Kok, J. F. (2011a). A scaling theory for the size distribution of emitted dust aerosols suggests climate models underestimate the size of the global dust cycle. *Proceedings of the National Academy of Science USA*, 108, 1016–1021. <https://doi.org/https://doi.org/10.1073/pnas.1014798108>
- Kok, J. F. (2011b). Does the size distribution of mineral dust aerosols depend on the wind speed at emission? *Atmospheric Chemistry and Physics*, 11(19), 10149–10156. <https://doi.org/10.5194/acp-11-10149-2011>
- Kok, J. F., Parteli, E., Michaels, T., & Karam, D. (2012). The physics of wind blown sand and dust. *Reports on Progress in Physics*, 75, 106901. <https://doi.org/10.1088/0034-4885/75/10/106901>
- Kok, J. F., Mahowald, N. M., Fratini, G., Gillies, J. A., Ishizuka, M., Leys, J. F., et al. (2014). An improved dust emission model - Part 1: Model description and comparison against measurements. *Atmospheric Chemistry and Physics*, 14(23). <https://doi.org/10.5194/acp-14-13023-2014>
- Kok, J. F., Albani, S., Mahowald, N. M., & Ward, D. S. (2014). An improved dust emission model - Part 2: Evaluation in the Community Earth System Model, with implications for the use of dust source functions. *Atmospheric Chemistry and Physics*, 14(23). <https://doi.org/10.5194/acp-14-13043-2014>
- Kok, J. F., Ridley, D. A., Zhou, Q., Miller, R. L., Zhao, C., Heald, C. L., et al. (2017). Smaller desert dust cooling effect estimated from analysis of dust size and abundance. *Nature Geoscience*, 10(4), 274–278. <https://doi.org/10.1038/ngeo2912>

- Kok, J. F., Adebisi, A. A., Albani, S., Balkanski, Y., Checa-Garcia, R., Chin, M., Colarco, P. R., Hamilton, D. S., Huang, Y., Ito, A., Klose, M., Li, L., et al. (2021). Contribution of the world's main dust source regions to the global cycle of desert dust. *Atmospheric Chemistry and Physics*, 21(10), 8169–8193. <https://doi.org/10.5194/acp-21-8169-2021>
- Kok, J. F., Adebisi, A. A., Albani, S., Balkanski, Y., Checa-Garcia, R., Chin, M., Colarco, P. R., Hamilton, D. S., Huang, Y., Ito, A., Klose, M., Leung, D. M., et al. (2021). Improved representation of the global dust cycle using observational constraints on dust properties and abundance. *Atmospheric Chemistry and Physics*, 21(10), 8127–8167. <https://doi.org/10.5194/acp-21-8127-2021>
- Kok, J. F., Storelvmo, T., Karydis, V. A., Adebisi, A. A., Mahowald, N. M., Evan, A. T., et al. (2023). Mineral dust aerosol impacts on global climate and climate change. *Nature Reviews Earth & Environment*. <https://doi.org/10.1038/s43017-022-00379-5>
- Langmann, B. (2013). Volcanic Ash versus Mineral Dust: Atmospheric Processing and Environmental and Climate Impacts. *ISRN Atmospheric Sciences, Article ID*, 1–17. <https://doi.org/10.1155/2013/245076>
- Lawrence, C. R., & Neff, J. (2009). The contemporary physical and chemical flux of Aeolian dust: a synthesis of direct measurements of dust deposition. *Chemical Geology*, 257, 46–63. <https://doi.org/https://doi.org/10.1016/j.chemgeo.2009.02.005>
- Leung, D. M., Kok, J. F., Li, L., Okin, G. S., Prigent, C., Klose, M., et al. (2023). A new process-based and scale-aware desert dust emission scheme for global climate models – Part I: Description and evaluation against inverse modeling emissions. *Atmospheric Chemistry and Physics*, (4), 6487–6523. <https://doi.org/10.5194/acp-23-6487-2023>
- Leung, D. M., Kok, J. F., Li, L., Mahowald, N. M., Lawrence, D. M., Tilmes, S., et al. (2024). A new process-based and scale-aware desert dust emission scheme for global climate models – Part II: Evaluation in the Community Earth System Model version 2 (CESM2). *Atmospheric Chemistry and Physics*, 24(4), 2287–2318. <https://doi.org/10.5194/acp-24-2287-2024>
- Levy, R. C., Remer, L. A., Kleidman, R. G., Mattoo, S., Ichoku, C., Kahn, R., & Eck, T. F. (2010). Global evaluation of the Collection 5 MODIS dark-target aerosol products over land. *Atmospheric Chemistry and Physics*, 10(21), 10399–10420. <https://doi.org/10.5194/acp-10-10399-2010>
- Li, L., & Sokolik, I. N. (2018). Analysis of dust aerosol retrievals using satellite data in Central Asia. *Atmosphere*, 9(8), 288-. <https://doi.org/10.3390/atmos9080288>
- Li, L., Mahowald, N. M., Miller, R. L., Pérez García-Pando, C., Klose, M., Hamilton, D. S., et al. (2021). Quantifying the range of the dust direct radiative effect due to source mineralogy uncertainty. *Atmospheric Chemistry and Physics*, 21(5), 3973–4005. <https://doi.org/10.5194/acp-21-3973-2021>
- Li, L., Mahowald, N. M., Kok, J. F., Liu, X., Wu, M., Leung, D. M., et al. (2022). Importance of different parameterization changes for the updated dust cycle modeling in the Community Atmosphere Model (version 6.1). *Geoscientific Model Development*, 15(22), 8181–8219. <https://doi.org/10.5194/gmd-15-8181-2022>

- Li, L., Mahowald, N. M., Gonçalves Ageitos, M., Obiso, V., Miller, R. L., Pérez García-Pando, C., et al. (2024). Improved constraints on hematite refractive index for estimating climatic effects of dust aerosols. *Communications Earth and Environment*, 5(1). <https://doi.org/10.1038/s43247-024-01441-4>
- Li, L., Mahowald, N. M., Miller, R. L., Pérez García-Pando, C., Gonçalves Ageitos, M., Ginoux, P., et al. (2025). *Spaceborne mineral mapping reduces dust's shortwave radiative impact uncertainty*. <https://doi.org/https://doi.org/10.31223/X57Q97>
- Liao, H., & Seinfeld, J. H. (1998). Radiative forcing by mineral dust aerosols: sensitivity to key variables. *Journal of Geophysical Research*, 103(D24), 31,631-637,645.
- Liu, X., Easter, R. C., Ghan, S. J., Zaveri, R., Rasch, P., Shi, X., et al. (2012). Toward a minimal representation of aerosols in climate models: Description and evaluation in the Community Atmosphere Model CAM5. *Geoscientific Model Development*, 5(3), 709–739. <https://doi.org/10.5194/gmd-5-709-2012>
- Liu, X., Ma, P. L., Wang, H., Tilmes, S., Singh, B., Easter, R. C., et al. (2016). Description and evaluation of a new four-mode version of the Modal Aerosol Module (MAM4) within version 5.3 of the Community Atmosphere Model. *Geoscientific Model Development*, 9(2), 505–522. <https://doi.org/10.5194/gmd-9-505-2016>
- Longo, A. F., Feng, Y., Lai, B., Landing, W. M., Shelley, R. U., Nenes, A., et al. (2016). Influence of Atmospheric Processes on the Solubility and Composition of Iron in Saharan Dust. *Environmental Science and Technology*, 50(13), 6912–6920. <https://doi.org/10.1021/acs.est.6b02605>
- Lu, L., Li, L., Rathod, S., Hess, P., Martínez, C., Fernandez, N., et al. (2024). Characterizing the Atmospheric Mn Cycle and Its Impact on Terrestrial Biogeochemistry. *Global Biogeochemical Cycles*, 38(4). <https://doi.org/10.1029/2023GB007967>
- Luo, C., Mahowald, N., Bond, T., Chuang, P. Y., Artaxo, P., Siefert, R., et al. (2008). Combustion iron distribution and deposition. *Global Biogeochemical Cycles*, 22(1). <https://doi.org/10.1029/2007GB002964>
- Mahowald, N. M. (2011). Aerosol Indirect Effect on Biogeochemical Cycles and Climate. *Science*, 334(November), 1500.
- Mahowald, N. M., Baker, A. R. A. R., Bergametti, G., Brooks, N., Duce, R. A. R. A., Jickells, T. D. T. D., et al. (2005). Atmospheric global dust cycle and iron inputs to the ocean. *Global Biogeochemical Cycles*, 19(4), GB4025. <https://doi.org/10.1029/2004GB002402>
- Mahowald, N M, D. Muhs, Levis, S., Rasch, P. J., Yoshioka, M., Zender, C. S., et al. (2006). Change in atmospheric mineral aerosols in response to climate: last glacial period, pre-industrial, modern and doubled-carbon dioxide climates . *Journal of Geophysical Research*, 111(10), D10202, doi:10.1029/2005JD006653. <https://doi.org/10.1029/2005JD006653>
- Mahowald, N. M., D. Muhs, Levis, S., Rasch, P. J., Yoshioka, M., Zender, C. S., et al. (2006). Change in atmospheric mineral aerosols in response to climate: last glacial period, pre-industrial, modern and doubled-carbon dioxide climates . *Journal of Geophysical Research*, 111(10), D10202, doi:10.1029/2005JD006653. <https://doi.org/10.1029/2005JD006653>

- 1711 Mahowald, N. M., Kloster, S., Engelstaedter, S., Moore, J. K., Mukhopadhyay, S., McConnell, J. R., et al. (2010).
1712 Observed 20th century desert dust variability: Impact on climate and biogeochemistry. *Atmospheric Chemistry*
1713 *and Physics*, 10(22), 10875–10893. <https://doi.org/10.5194/acp-10-10875-2010>
- 1714 Mahowald, N. M., Albani, S., Kok, J. F., Engelstaeder, S., Scanza, R., Ward, D. S., & Flanner, M. G. (2014). The
1715 size distribution of desert dust aerosols and its impact on the Earth system. *Aeolian Research*, 15.
1716 <https://doi.org/10.1016/j.aeolia.2013.09.002>
- 1717 Mahowald, N. M., Hamilton, D. S., Mackey, K. R. M., Moore, J. K., Baker, A. R., Scanza, R. A., & Zhang, Y.
1718 (2018). Aerosol trace metal leaching and impacts on marine microorganisms. *Nature Communications*, 9(1).
1719 <https://doi.org/10.1038/s41467-018-04970-7>
- 1720 Mahowald, N. M., Li, L., Albani, S., Hamilton, D. S., & Kok, J. F. (2024). Opinion: The importance of historical
1721 and paleoclimate aerosol radiative effects. *Atmospheric Chemistry and Physics*, 24, 533–551.
1722 <https://doi.org/10.5194/acp-24-533-2024>
- 1723 Mahowald, N. M., Li, L., Vira, J., Prank, M., Hamilton, D. S., Matsui, H., et al. (2025). AERO-MAP: a data
1724 compilation and modeling approach to understand spatial variability in fine- and coarse-mode aerosol
1725 composition. *Atmospheric Chemistry and Physics*, 25(9), 4665–4702. [https://doi.org/10.5194/acp-25-4665-](https://doi.org/10.5194/acp-25-4665-2025)
1726 2025
- 1727 Mahowald, Natalie M., Engelstaedter, S., Luo, C., Sealy, A., Artaxo, P., Benitez-Nelson, C., et al. (2009).
1728 Atmospheric Iron Deposition: Global Distribution, Variability, and Human Perturbations. *Annual Review of*
1729 *Marine Science*, 1(1), 245–278. <https://doi.org/10.1146/annurev.marine.010908.163727>
- 1730 Maki, T., Noda, J., Morimoto, K., Aoki, K., Kurosaki, Y., Huang, Z., et al. (2022). Long-range transport of airborne
1731 bacteria over East Asia: Asian dust events carry potentially nontuberculous Mycobacterium populations.
1732 *Environment International*, 168. <https://doi.org/10.1016/j.envint.2022.107471>
- 1733 Mallios, S. A., Drakaki, E., & Amiridis, V. (2020). Effects of dust particle sphericity and orientation on their
1734 gravitational settling in the earth’s atmosphere. *Journal of Aerosol Science*, 150(April), 1–21.
1735 <https://doi.org/10.1016/j.jaerosci.2020.105634>
- 1736 Marticorena, B., & Bergametti, G. (1995). Modeling the atmospheric dust cycle: 1. Design of a soil-derived dust
1737 emission scheme. *Journal of Geophysical Research*, 100(D8), 16,415-16,430.
1738 <https://doi.org/https://doi.org/10.1029/95JD00690>
- 1739 Mccutcheon, J., Lutz, S., Williamson, C., Joseph, M., Tedstone, A. J., Vanderstraeten, A., et al. (2021). Mineral
1740 phosphorus drives glacier algal blooms on the Greenland Ice Sheet. *Nature Communications*, (2021), 1–11.
1741 <https://doi.org/10.1038/s41467-020-20627-w>
- 1742 Measures, C. I., & Vink, S. (2000). On the use of dissolved aluminum in surface waters to estimate dust deposition
1743 to the ocean. *Global Biogeochemical Cycles*, 14(1), 317–327. <https://doi.org/10.1029/1999GB001188>

- 1744 Meinander, O., Dagsson-Waldhauserova, P., Amosov, P., Aseyeva, E., Atkins, C., Baklanov, A., et al. (2022).
1745 Newly identified climatically and environmentally significant high-latitude dust sources. *Atmospheric*
1746 *Chemistry and Physics*, 22(17), 11889–11930. <https://doi.org/10.5194/acp-22-11889-2022>
- 1747 Meng, J., Huang, Y., Leung, D. M., Li, L., Adebiyi, A. A., Ryder, C. L., et al. (2022). Improved Parameterization
1748 for the Size Distribution of Emitted Dust Aerosols Reduces Model Underestimation of Super Coarse Dust.
1749 *Geophysical Research Letters*, 49(8), 1–12. <https://doi.org/10.1029/2021GL097287>
- 1750 Meskhidze, N., Chameides, W. L., & Nenes, A. (2005). Dust and pollution: A recipe for enhanced ocean
1751 fertilization? *Journal of Geophysical Research D: Atmospheres*, 110(3), 1–23.
1752 <https://doi.org/10.1029/2004JD005082>
- 1753 Neale, R. B., Chen, C., Lauritzen, P. H., Williamson, D. L., Conley, A. J., Smith, A. K., et al. (2010). *Description of*
1754 *the NCAR Community Atmosphere Model (CAM 5.0)*. NCAR Technical note. Boulder, CO.
- 1755 Niimura, N., Okada, K., Fan, X.-B., Kai, K., Arao, K., Shi, G.-Y., & Takahashi, S. (1998). Formation of Asian dust-
1756 storm particles mixed internally with sea salt in the atmosphere. *Journal of the Meteorological Society of*
1757 *Japan*, 76(2), 275–288. https://doi.org/10.2151/jmsj1965.76.2_275
- 1758 Obiso, V., Gonçalves Ageitos, M., Pérez García-Pando, C., Perlwitz, J. P., Schuster, G. L., Bauer, S. E., et al.
1759 (2024). Observationally constrained regional variations of shortwave absorption by iron oxides emphasize the
1760 cooling effect of dust. *Atmospheric Chemistry and Physics*, 24(9), 5337–5367. [https://doi.org/10.5194/acp-24-](https://doi.org/10.5194/acp-24-5337-2024)
1761 [5337-2024](https://doi.org/10.5194/acp-24-5337-2024)
- 1762 Okin, G. (2008). A new model of wind erosion in the presence of vegetation. *Journal of Geophysical Research*,
1763 113(F02S10), 1–11. <https://doi.org/10.1029/2007JF000758>
- 1764 Okin, G. S., Ochoa, F., Brodrick, P. G., Thompson, D. R., Keebler, A., Ehlmann, B. L., et al. (2023). *EMIT L3*
1765 *Algorithm: Aggregated Mineral Spectral Abundance Theoretical Basis*. Pasadena, California 91109-8099.
- 1766 Osada, K. (2013). Water soluble fraction of Asian dust particles Laser Intensity Before Height μ m After.
1767 *Atmospheric Research*, 124, 101–108. <https://doi.org/10.1016/j.atmosres.2013.01.001>
- 1768 Panta, A., Kandler, K., Alastuey, A., González-Flórez, C., González-Romero, A., Klose, M., et al. (2023). Insights
1769 into the single particle composition, size, mixing state and aspect ratio of freshly emitted mineral dust from
1770 field measurements in the Moroccan Sahara using electron microscopy. *Atmospheric Chemistry and Physics*,
1771 23, 3861–3885. <https://doi.org/10.5194/acp-23-3861-2023>
- 1772 Pérez García-Pando, C., Stanton, M. C., Diggle, P. J., Trzaska, S., & Miller, R. L. (2014). Soil Dust Aerosols and
1773 Wind as Predictors of Seasonal Meningitis Incidence. *Environ Health Perspect*, 122(7), 679–686.
- 1774 Perlwitz, J. P., Pérez García-Pando, C., & Miller, R. L. (2015a). Predicting the mineral composition of dust aerosols
1775 - Part 1: Representing key processes. *Atmospheric Chemistry and Physics*, 15(20), 11593–11627.
1776 <https://doi.org/10.5194/acp-15-11593-2015>

- 1777 Perlwitz, J. P., Pérez García-Pando, C., & Miller, R. L. (2015b). Predicting the mineral composition of dust aerosols
1778 - Part 2: Model evaluation and identification of key processes with observations. *Atmospheric Chemistry and*
1779 *Physics*, 15(20), 11629–11652. <https://doi.org/10.5194/acp-15-11629-2015>
- 1780 Petroff, A., & Zhang, L. (2010). Development and validation of a size-resolved particle dry deposition scheme for
1781 application in aerosol transport models. *Geosci. Model Dev.*, 3, 753–769. [https://doi.org/10.5194/gmd-3-753-](https://doi.org/10.5194/gmd-3-753-2010)
1782 2010
- 1783 Pierre, C., Bergametti, G., Marticorena, B., Kergoat, L., Mougin, E., & Hiernaux, P. (2014). Comparing drag
1784 partition schemes over a herbaceous Sahelian rangeland. *Journal of Geophysical Research: Earth Surface*,
1785 119, 2291–2313. <https://doi.org/10.1002/2014JF003177>
- 1786 Prigent, C., Tegen, I., Aires, F., Marticorena, B., & Zribi, M. (2005). Estimation of the aerodynamic roughness
1787 length in arid and semi-arid regions over the globe with the ERS scatterometer. *Journal of Geophysical*
1788 *Research D: Atmospheres*, 110(9), 1–12. <https://doi.org/10.1029/2004JD005370>
- 1789 Prospero, J. M., Bonatti, E., Schubert, C., & Carlson, T. N. (1970). Dust in the Caribbean atmosphere traced to an
1790 African dust storm. *Earth Planetary Science Letters*, 9, 287–293. [https://doi.org/10.1016/0012-](https://doi.org/10.1016/0012-821X(70)90039-7)
1791 821X(70)90039-7
- 1792 Prospero, J. M., Olmez, I., & Ames, M. (2001). Al and Fe in PM 2.5 and PM 10 Suspended Particles in South-
1793 Central Florida: The Impact of the Long Range Transport of African Mineral Dust. *Water, Air, & Soil*
1794 *Pollution*, 125, 291–317. <https://doi.org/10.1023/A:1005277214288>
- 1795 Ratcliffe, N. G., Ryder, C. L., Bellouin, N., Woodward, S., Jones, A., Johnson, B., et al. (2024). Long-range
1796 transport of coarse mineral dust: an evaluation of the Met Office Unified Model against aircraft observations.
1797 *Atmospheric Chemistry and Physics*, 24(21), 12161–12181. <https://doi.org/10.5194/acp-24-12161-2024>
- 1798 Reid, E., Reid, J., Meier, M., Dunlap, M., Cliff, S., Broumas, A., et al. (2003). Characterization of African dust
1799 transported to Puerto Rico by individual particle and size segregated bulk analysis. *Journal of Geophysical*
1800 *Research*, 108(D198591), 1–22. <https://doi.org/doi:10.1029/2000JD002935>
- 1801 Reid, J. S., Westphal, D. L., Livingston, J. M., Savoie, D. L., Maring, H. B., Jonsson, H. H., et al. (2002). Dust
1802 vertical distribution in the Caribbean during the Puerto Rico Dust experiment. *Geophysical Research Letters*,
1803 29(7), 1–4. <https://doi.org/10.1029/2001GL014092>
- 1804 Reid, J. S., Jonsson, H. H., Maring, H. B., Smirnov, A., Savoie, D. L., Cliff, S. S., et al. (2003). Comparison of size
1805 and morphological measurements of coarse mode dust particles from Africa. *Journal of Geophysical Research*
1806 *D: Atmospheres*, 108(D19). <https://doi.org/10.1029/2002jd002485>
- 1807 Ridley, A. D., Heald, L. C., Kok, F. J., & Zhao, C. (2016). An observationally constrained estimate of global dust
1808 aerosol optical depth. *Atmospheric Chemistry and Physics*, 16(23), 15097–15117. [https://doi.org/10.5194/acp-](https://doi.org/10.5194/acp-16-15097-2016)
1809 16-15097-2016

- Rodakoviski, R., Kok, J., & Chamecki, M. (2023). Dust Settling From Turbulent Layers in the Free Troposphere: Implications for the Saharan Air Layer. *Journal of Geophysical Research: Atmospheres*, 128(6). <https://doi.org/10.1029/2022JD037724>
- Rosenberg, P., Parker, D., Ryder, C., Marsham, J., Garcia-Carreras, L., Dorsey, J., et al. (2014). Quantifying particle size and turbulent scale dependence of dust flux in the Sahara using air craft measurements. *Journal of Geophysical Research*, 119, 7577–7598; doi: 10.1002/2013JD021255.
- Ryder, C. L., Highwood, E. J., Rosenberg, P. D., Trembath, J., Brooke, J. K., Bart, M., et al. (2013). Optical properties of Saharan dust aerosol and contribution from the coarse mode as measured during the Fennec 2011 aircraft campaign. *Atmospheric Chemistry and Physics*, 13(1), 303–325. <https://doi.org/10.5194/acp-13-303-2013>
- Ryder, C. L., Highwood, E. J., Walser, A., Seibert, P., Philipp, A., & Weinzierl, B. (2019). Coarse and giant particles are ubiquitous in Saharan dust export regions and are radiatively significant over the Sahara. *Atmospheric Chemistry and Physics*, 19(24), 15353–15376. <https://doi.org/10.5194/acp-19-15353-2019>
- Ryder, Claire L., Marengo, F., Brooke, J. K., Estelles, V., Cotton, R., Formenti, P., et al. (2018). Coarse-mode mineral dust size distributions, composition and optical properties from AER-D aircraft measurements over the tropical eastern Atlantic. *Atmospheric Chemistry and Physics*, 18(23), 17225–17257. <https://doi.org/10.5194/acp-18-17225-2018>
- Scanza, R. A., Mahowald, N., Ghan, S., Zender, C. S., Kok, J. F., Liu, X., et al. (2015). Modeling dust as component minerals in the Community Atmosphere Model: Development of framework and impact on radiative forcing. *Atmospheric Chemistry and Physics*, 15(1). <https://doi.org/10.5194/acp-15-537-2015>
- Shao, Y. (2008). *Physics and Modelling of Wind Erosion. Physics and Modelling of Wind Erosion* (2nd ed.). Heidelberg: Springer. <https://doi.org/10.1007/978-1-4020-8895-7>
- Shi, X., Liu, X., & Zhang, K. (2015). Effects of pre-existing ice crystals on cirrus clouds and comparison between different ice nucleation parameterizations with the Community Atmosphere Model (CAM5). *Atmospheric Chemistry and Physics*, 15(3), 1503–1520. <https://doi.org/10.5194/acp-15-1503-2015>
- Shi, Y., Liu, X., Wu, M., Ke, Z., & Brown, H. (2021). Relative Importance of High-Latitude Local and Long-Range Transported Dust to Arctic Ice Nucleating Particles and Impacts on Arctic Mixed-Phase Clouds. *Atmospheric Chemistry and Physics Discussions*, (August), 1–57. <https://doi.org/10.5194/acp-2021-621>
- Shinn, E., Smith, G., Prospero, J., Betzer, P., Hayes, M., Garrison, V., & Barber, R. (2000). African dust and the demise of the Caribbean Coral Reefs. *Geophysical Research Letters*, 27(19), 3029–3032.
- Sokolik, I. N., & Toon, O. B. (1999). Incorporation of mineralogical composition into models of the radiative properties of mineral aerosol from UV to IR wavelengths. *Journal of Geophysical Research Atmospheres*, 104(D8), 9423–9444. <https://doi.org/10.1029/1998JD200048>
- Stokes, G. G. (1851). On the effect of the internal friction of fluids on the motion of a pendulum. *Transactions of the Cambridge Philosophical Society*, 8(9).

- 1845 Tegen, I., Harrison, S. P., Kohfeld, K., Prentice, C., Coe, M., & Heimann, M. (2002). The impact of vegetation and
1846 preferential source areas on global dust aerosol: Results from a model study. *Journal of Geophysical*
1847 *Research*, 107(D21), 4576–4597. <https://doi.org/https://doi.org/10.1029/2001JD000963>
- 1848 Thompson, D. R., Green, R. O., Bradley, C., Brodrick, P. G., Mahowald, N., Dor, E. Ben, et al. (2024). On-orbit
1849 calibration and performance of the EMIT imaging spectrometer. *Remote Sensing of Environment*, 303.
1850 <https://doi.org/10.1016/j.rse.2023.113986>
- 1851 Toth, J. R., Rajupet, S., Squire, H., Volbers, B., Zhou, J., Xie, L., et al. (2020). Electrostatic forces alter particle size
1852 distributions in atmospheric dust. *Atmospheric Chemistry and Physics*, 20(5), 3181–3190.
1853 <https://doi.org/10.5194/acp-20-3181-2020>
- 1854 Usher, C. R., Michel, A. E., & Grassian, V. H. (2003). Reactions on Mineral Dust. *Chemical Reviews*, 103(12),
1855 4883–4939. <https://doi.org/10.1021/cr020657y>
- 1856 Wan, H., Zhang, K., Vogl, C. J., Woodward, C. S., Easter, R. C., Rasch, P. J., et al. (2024). Numerical coupling of
1857 aerosol emissions, dry removal, and turbulent mixing in the E3SM Atmosphere Model version 1 (EAMv1) –
1858 Part 1: Dust budget analyses and the impacts of a revised coupling scheme. *Geoscientific Model Development*,
1859 17(3), 1387–1407. <https://doi.org/10.5194/gmd-17-1387-2024>
- 1860 Wang, H., Liu, X., Wu, C., Lin, G., Dai, T., Goto, D., et al. (2024). Larger Dust Cooling Effect Estimated From
1861 Regionally Dependent Refractive Indices. *Geophysical Research Letters*, 51(9).
1862 <https://doi.org/10.1029/2023GL107647>
- 1863 Warren, S. G., Roesler, C. S., Brandt, R. E., & Curran, M. (2019). Green Icebergs Revisited Journal of Geophysical
1864 Research : Oceans. *Journal of Geophysical Research: Oceans*, 124, 925–938.
1865 <https://doi.org/10.1029/2018JC014479>
- 1866 Weinzierl, B., Ansmann, A., Prospero, J. M., Althausen, D., Benker, N., Chouza, F., et al. (2017). The Saharan
1867 aerosol long-range transport and aerosol-cloud-interaction ex- periment: Overview and selected highlights.
1868 *Bulletin American Meteorological Society*, 98, 1427–1452. <https://doi.org/10.1175/BAMS-D-15-00142.1>
- 1869 Weinzierl, Bernadett, Petzold, A., Esselborn, M., Wirth, M., Rasp, K., Kandler, K., et al. (2009). Airborne
1870 measurements of dust layer properties, particle size distribution and mixing state of Saharan dust during
1871 SAMUM 2006. *Tellus, Series B: Chemical and Physical Meteorology*, 61(1), 96–117.
1872 <https://doi.org/10.1111/j.1600-0889.2008.00392.x>
- 1873 Wong, M. Y., Rathod, S. D., Marino, R., Li, L., Howarth, R. W., Alastuey, A., et al. (2021). Anthropogenic
1874 Perturbations to the Atmospheric Molybdenum Cycle. *Global Biogeochemical Cycles*, 35(2).
1875 <https://doi.org/10.1029/2020GB006787>
- 1876 Wu, M., Liu, X., Zhang, L., Wu, C., Lu, Z., Ma, P. L., et al. (2018). Impacts of Aerosol Dry Deposition on Black
1877 Carbon Spatial Distributions and Radiative Effects in the Community Atmosphere Model CAM5. *Journal of*
1878 *Advances in Modeling Earth Systems*, 10(5), 1150–1171. <https://doi.org/10.1029/2017MS001219>

- Zender, C., Bian, H., & Newman, D. (2003). Mineral Dust Entrainment and Deposition (DEAD) model: Description and 1990s dust climatology. *Journal of Geophysical Research*, 108(D14), 4416, doi:10.1029/2002JD002775.
- Zender, C., Newman, D., & Torres, O. (2003). Spatial Heterogeneity in Aerolian Erodibility: Uniform, Topographic, Geomorphic and Hydrologic Hypotheses. *Journal of Geophysical Research*, 108(D17), 4543, doi:10.1029/2002JD003039.
- Zhang, L., Gong, S., Padro, J., & Barrie, L. (2001). A size-segregated particle dry deposition scheme for an atmospheric aerosol module. *Atmospheric Environment*, 35(3), 549–560. [https://doi.org/10.1016/S1352-2310\(00\)00326-5](https://doi.org/10.1016/S1352-2310(00)00326-5)
- Zheng, J., Zhang, Z., Garnier, A., Yu, H., Song, Q., Wang, C., et al. (2022). The thermal infrared optical depth of mineral dust retrieved from integrated CALIOP and IIR observations. *Remote Sensing of Environment*, 270. <https://doi.org/10.1016/j.rse.2021.112841>